



Review

Modified metal-organic frameworks as photocatalysts

Jianhao Qiu^a, Xingguang Zhang^a, Yi Feng^a, Xiongfei Zhang^a, Huanting Wang^{b,*}, Jianfeng Yao^{a,*}^a College of Chemical Engineering, Jiangsu Key Lab for the Chemistry & Utilization of Agricultural and Forest Biomass, Nanjing Forestry University, 159 Longpan Road, Nanjing, 210037, Jiangsu, PR China^b Department of Chemical Engineering, Monash University, Clayton, Victoria 3800, Australia

ARTICLE INFO

Keywords:
 Metal-organic framework
 Photocatalyst
 Modification
 Application

ABSTRACT

Photocatalysis is a promising and ideal technology to utilize solar energy for energy regeneration and environmental remediation. Photocatalysis based on metal-organic frameworks (MOFs) has attracted extensive attention because of their excellent properties such as tunable structure and optical properties. This review principally summarizes the progress of various modification strategies, including decoration of organic linker or metal center, combination with semiconductors and metal nanoparticles loading, applied to different MOFs (mainly UiOs, MILs, and ZIFs), and their specific applications were summarized as well. In addition, the existing problems and the development prospect of MOFs for photocatalysis were also presented.

1. Introduction

Photocatalysis is a convenient and environmental-friendly approach to convert solar energy into chemical energy. Great progress has been made since the pioneering work on solar energy conversion using TiO_2 photocatalysts reported by Fujishima and Honda in 1972 [1]. From nature photosynthesis to artificial employment of the solar energy, photocatalysis plays an increasingly important role in many fields, such as clean chemicals synthesis, environmental remediation (e.g. degradation of organic dyes [2,3], reduction of heavy metal ions in wastewater [4], and inhibition of air pollutants [5]) energy regeneration (e.g. splitting of water into H_2 [6,7], and CO_2 photocatalytic reduction into solar fuels [8,9]). Researchers have already developed numerous materials as the photocatalysts, and the earliest study is based on the TiO_2 semiconductor material [10,11] and its modification [12,13]. Meanwhile, some novel photocatalytic semiconductors have emerged, such as $\text{g-C}_3\text{N}_4$ [14–16], ZnO [17,18], Ag_3PO_4 [19,20] and their composites [21,22]. However, the large band gap and the ready recombination of electron-hole pairs lead to low photocatalytic efficiency and poor practicality; moreover, the non-adjustable structure of conventional semiconductor materials limited their further

development in the field of photocatalysis. Therefore, it is highly imperative to explore efficient, robust and cost-effective photocatalytic materials to replace the traditional ones.

Owing to the large surface areas, well-ordered porous structures and tunable organic linkers or metal clusters, the newly emerged functional inorganic-organic hybrid materials of metal-organic frameworks (MOFs) [23,24] have attracted considerable interest in numerous fields, such as gas storage [25,26], separation [27–29], drug delivery [30], chemical sensors [31] and heterogeneous catalysis [32–35]. Among heterogeneous catalysis, utilizing MOFs for photocatalysis is a very significant work in the future [36,37], which is mainly based on two aspects: (1) Pristine MOFs as photocatalysts. These porous materials can act as catalysts themselves not only because the above-mentioned physical merits but also the chemical advantages (existence of open metal sites, unsaturated metal centers and even the catalytically active organic linkers [38]). In addition, some MOFs can act as semiconductors (e.g. MOF-5 [39], NTU-9 [40] and UIO-66 [41–43]), wherein the energy transfer takes place from the organic linker to the metal-oxo cluster. However, most MOFs as photocatalysts possess a large band gap that can merely harvest UV light, which immensely limits their further application. (2) Modified MOFs as photocatalysts.

Abbreviations: MOF, metal-organic framework; UIO, University of Oslo; MIL, Materials of Institut Lavoisier; ZIF, zeolitic imidazolate framework; VB, valence band; CB, conduction band; HOMO, highest occupied molecular orbital; LUMO, lowest unoccupied molecular orbital; UV, ultraviolet; UV-vis, ultraviolet-visible; OG, orange G; RhB, rhodamine B; RBBR, Remazol Brilliant Blue R; MB, methylene blue; MO, methyl orange; ErB, Erythrosin B; Rh6G, rhodamine 6G; DRS, diffuse reflective spectra; DOS, density of states; LMCT, ligand-to-metal charge transfer; BDC, terephthalic acid; MNP, metal nanoparticle; GR, graphene; RGO, reduced graphene oxide; SBU, secondary building unites; PC, pyridinecarboxaldehyde; PSE, post-synthetic exchange; DFT, density functional theory; ESR, electron spin resonance; ATA, 2-aminoterephthalic acid; CNNS, carbon nitride nanosheet; PANI, polyaniline; SPR, surface plasmon resonance; PCVG, photochemical vapor generation; PHIK, heptazine imide; AC, acetylacetone; CoIIIBr₂(LH), co-dioxime-diimine; MOCVD, metal-organic chemical vapor deposition; POM, polyoxometalate; PPCP, pharmaceutical and personal care product; MAG-MIL, magnetic MIL-53(Fe); TEOA, triethanolamine; NC, nanocube; PEC, photoelectrochemical; OER, oxygen evolution reaction; BP, black phosphorus; PMS, peroxymonosulfate; TEM, transmission electron microscope; SEM, scanning electron microscope

* Corresponding authors.

E-mail addresses: huanting.wang@monash.edu (H. Wang), jfyao@njfu.edu.cn (J. Yao).

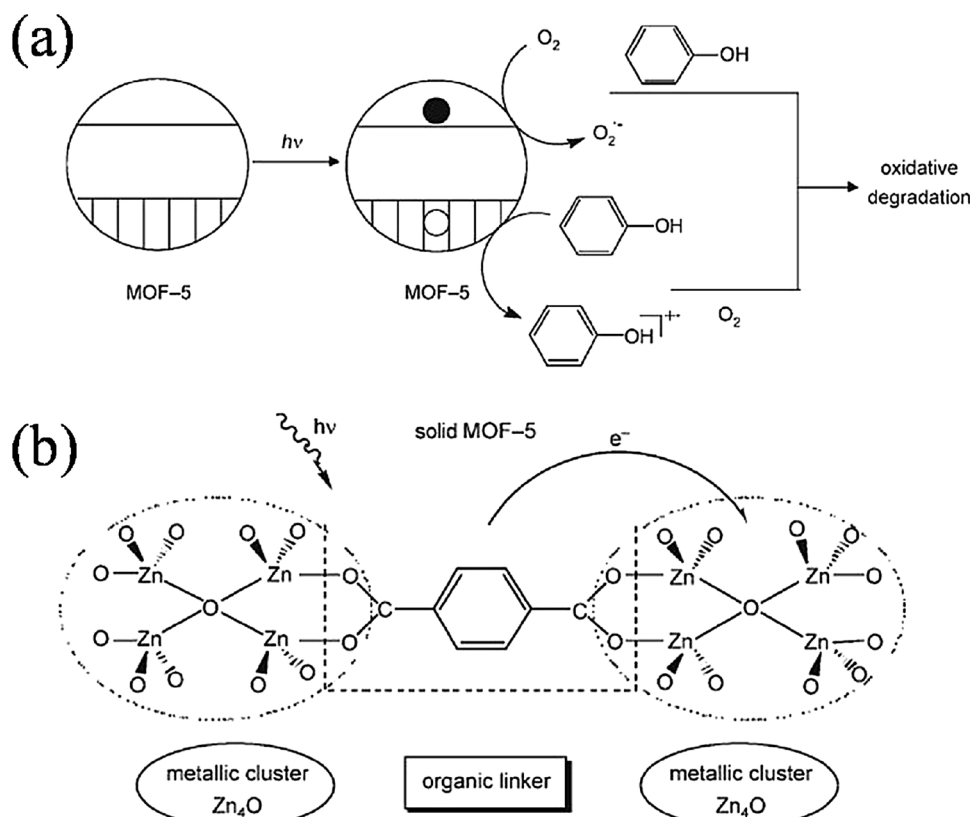


Fig. 1. The possible mechanism of oxidative photocatalytic degradation by MOF-5 (a) and photophysical processes that occur after the irradiation of the MOF-5 solid material (b) [52].

There are several different strategies, including decoration of linker or metal center [44,45], combination with semiconductors [41,46] and sensitization by such as dyes [42,43]. This way is particularly important because it extensively functionalizes MOFs for visible light-induced photocatalysis, thereby leading to a far-reaching development of MOFs as photocatalysts.

Therefore, this review mainly concentrates on the state-of-the-art advance of MOFs-based photocatalysts, covering the representative MOFs such as UiOs, MILs and ZIFs, modification strategies, and their applications. Finally, the existing problems of the existent MOFs photocatalysts are pointed out and the future perspectives are proposed.

2. Pristine MOFs

A semiconductor photocatalyst has its band gap. When the energy provided by light illumination is higher than the band gap energy, the negative electrons (e^-) in the valence band (VB) will move to the conduction band (CB), generating positive holes (h^+) in the VB, and then the reduction and oxidation half reactions with the electrons and holes will be taken place respectively (Fig. 1a) [47,48]. As for MOFs, the organic linker is regarded as VB and the metallic cluster plays the role of CB (Fig. 1b). Specially, the process for an organic semiconductor is also described as occurring between the highest occupied molecular orbital (HOMO) and the lowest unoccupied molecular orbital (LUMO) [49–51]. The development of pristine MOFs as photocatalysts is from ultraviolet (UV) -light-driven ($E_g > 3.1$ eV, $\lambda < 400$ nm) to visible-light-driven ($E_g < 3.1$ eV, $\lambda > 400$ nm).

The initial attempts of MOFs utilized in photocatalytic reactions are under UV-light irradiation. The first example of MOFs as a photocatalyst is Mahata and the co-workers' report, in which three new coordination polymers ($[Co_2(C_{10}H_8N_2)]_2[C_{12}H_8O(COO)_2]_2$, $[Zn_2(C_{10}H_8N_2)]_2[C_{12}H_8O(COO)_2]_2$ and $[Ni_2(C_{10}H_8N_2)]_2[C_{12}H_8O(COO)_2]_2 \cdot H_2O$) were examined for the degradation of orange G (OG), rhodamine B (RhB), Remazol Brilliant Blue R (RBBR) and methylene blue (MB) under

the irradiation of mercury vapor lamp [53]. The catalytic activities of three MOFs followed the reverse order to their band gaps. In 2007, Garcia and co-workers studied the photocatalytic properties of MOF-5(Zn) in the degradation of phenol and proved that MOF-5 exhibited reverse shape-selectivity [39,52]. Furthermore, they found the terephthalate linkers could absorb light and sensitized the semiconductor dots. To further investigate the influence of organic linkers on the photocatalytic activity of MOF-5, Gascon and co-workers demonstrated that the band gap energy of metal-organic frameworks can be tuned by changing the organic linker (Fig. 2) [54]. They found that using the 2,6-naphthalenedicarboxylic acid as a linker performed the best catalytic activity in the photooxidation of propene. Although there were other more studies focused on MOF-5 as photocatalysts [52,55], it would

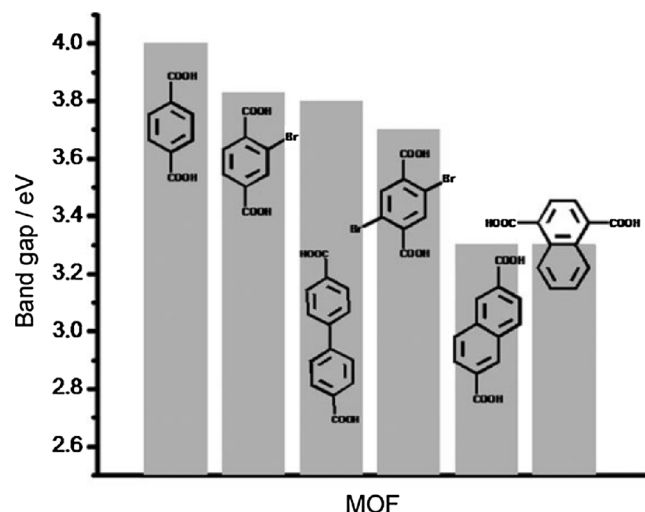


Fig. 2. The band gap value of different linkers of MOFs [54].

suffer structure transformation when exposed to water [56], and this structural change impaired the photocatalytic property. However, water is inevitable in some photocatalytic processes, such as the hydrogen generation in water and wastewater treatment. Therefore, to strengthen the stability of MOFs, especially in water is an important goal.

UiO-66 is a typical water-tolerant Zr-containing MOF. The first report on UiO-66 utilized in photocatalysis was for hydrogen generation in water/methanol upon irradiation at wavelength longer than 300 nm [44]. According to the laser flash photolysis data, the charge separation with electrons in the conduction band happens upon photon absorption. Although the apparent quantum yield was low and the band gap energy of UiO-66 (3.5 eV) is wide, such pioneering work opens ways for various modifications to UiO-66 for visible-light photocatalysis. Later in 2015, a UiO-66-type zirconium MOF using chromophoric anthracene-9,10-dicarboxylic acid instead of terephthalate acid (H₂BDC) was synthesized and performed efficiently in the visible-light-driven photocatalytic degradation of MO [57]. Jing and co-workers utilized ZIF-8 for the degradation of MB under UV-light irradiation [58]. They proved that the photocatalytic activity of ZIF-8 could work effectively over a wide pH range, especially in strong alkaline environment. However, the wide band gap of ZIF-8 (5.1 eV) limits the applications for photocatalysis to some degree.

MOFs containing Ti has attracted huge attention. In 2009, MIL-125(Ti) was synthesized by Dan-Hardi and co-workers for the first time [59]. The hybrid material exhibited high photonic sensitivity for the formation of Ti(III)-Ti(IV) mixed valence under UV-vis irradiation in the presence of alcohols, and the reduction of titanium centers and oxidation of absorbed alcohol molecules occurred simultaneously. Recently, MIL-125 was rapidly synthesized via a microwave route by George and co-workers [60]. The MIL-125 had a band gap energy of 3.14 eV and could degrade MB to ca. 96.77% in 6 h under UV-light irradiation.

Although an increasing number of MOFs appeared for photocatalysis, the large band gaps limited their utilization under visible light. It has stimulated researchers to develop novel MOFs with a reduced band gap to enhance the activity under visible-light irradiation. Das and co-workers synthesized a doubly interpenetrated semiconducting MOF $Zn_4O(2,6-NDC)_3\cdot(DMF)_{1.5}(H_2O)_{0.5}\cdot4DMF\cdot7.5H_2O$ (UTSA-38) for the methyl orange (MO) degradation [61]. The UV-vis diffuse reflective spectra (DRS) of UTSA-38 presented that it is a semiconductor MOF with a band gap of 2.85 eV. MIL-53 is a series of isostructural materials with the same organic linkers but different metal centers including Fe, Al and Cr. Among them, the MIL-53(Fe) possesses a narrow band gap of about 2.72 eV [51]. MIL-53(Fe) performed better photocatalytic activity for MB decolorization both under UV-light and visible-light irradiation. After a few years, MIL-53(Fe) got the further researches in the Cr(VI) reduction, dyes degradation and photoelectrochemical water oxidation under visible-light irradiation [62–64]. As the other typical visible-light responsive MOFs, MIL-100(Fe) has been synthesized for the selective benzene hydroxylation to phenol under visible-light irradiation using H₂O₂ as an oxidant (Fig. 3) [65]. A benzene conversion of 30.6% was achieved with a 3:4 ratio of H₂O₂:benzene over MIL-100 after 24 h. According to the ESR results and kinetic studies, the benzene hydroxylation process involved a coupling of Fe-O clusters in MIL-100 with a Fenton-like route. Besides, the structures of MOFs significantly influenced the photocatalytic efficiency. The MIL-100(M) (M = Al, Fe, V, Cr) with different metal centers has also been researched for MB photocatalytic degradation [66].

Although the aforementioned studies were both interesting and important, the MOFs could capture only a fraction of the photons in the visible spectrum. Toward this end, Lee and co-workers developed a pillared-paddlewheel type metal-organic framework featuring bodipy- and porphyrin-based struts, named BOP MOF (Fig. 4) [67]. The two struts in MOFs were a complementary pair of chromophores, in which the bodipy struts served as antenna chromophores for the excitation of

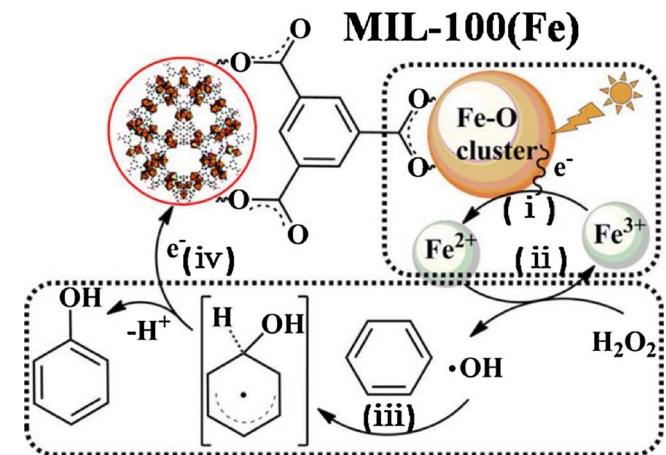


Fig. 3. Reaction mechanism for the photocatalytic benzene hydroxylation over MIL-100 [65].

porphyrinic struts. This BOP MOF could harvest light across the entire visible spectrum. Similarly, to utilize the advantage of small band gap of Iron (III) oxides and overcome the disadvantage of the high electron-hole recombination rate. MOFs containing Fe₃- μ_3 -oxo clusters were proposed as visible-light photocatalysts with the small particle dimensions and the remarkable photocatalytic efficiency of such Fe(III)-based MOFs were examined for the first time [68]. Later, other Fe(III)-based MOFs have also been investigated as photocatalysts for visible-light-driven O₂ evolution from water and benzene hydroxylation to form phenol [65,69].

Ti(IV)-based porous NTU-9 displayed stronger absorption in the visible light region than MIL-125 [40]. It shows a broad range of absorption in the visible region from 400 nm to 750 nm with a band gap of 1.72 eV (Fig. 5). The results of density of states (DOS) demonstrated the existence of charge transfer from the organic ligand to Ti(IV) atoms in NTU-9, which further proved the mechanism of ligand-to-metal charge transfer (LMCT) [39,67,70]. Crystalline NTU-9 is stable in air, water and common organic solvents. The photocatalytic activity was tested by the degradation of RhB and MB under visible-light irradiation ($\lambda > 420$ nm). RhB and MB were completely degraded for 80 min and 20 min, respectively (5 mg of NTU-9 was added in 10 mL of organic dyes (10^{-4} mol/L)). ZIF-67(Co) also has a broad light absorption, not only in the UV and visible-light region but also in the near IR region. The features were ascribed to the LMCT transition, the higher-lying [⁴A₂(F)-⁴T₁(P)] and lower-lying [⁴A₂(F)-⁴T₁(F)] d-d ligand field transitions, and Co²⁺ ions in T_d environment [71]. Optical transient absorption results showed that a long-lived excited state was formed after photo-excitation. Furthermore, the long-lived excited state was confirmed to be the charge-separated state with LMCT character according to X-ray transient absorption spectroscopy [72]. These characters suggested its potential application in heterogeneous photocatalysis [73] and energy conversion.

Pristine MOFs as photocatalysts were also called the “Opportunistic” photocatalysts [36], meaning that this type of photocatalysts are rare and hard to be readily tuned. Furthermore, most of pristine MOFs as photocatalysts are merely sensitive to UV light and the lifetimes of the excited states are too short to perform the catalytic activity, which limited the practicability under solar illumination. Pristine MOFs for photocatalysts and their corresponding applications are listed in Table 1. Besides, the exploitation of new MOFs that response to visible light is a challenging task. Therefore, modifications to MOFs would be a sensible choice.

3. UiOs

The rational designs and modifications of MOFs focus on two

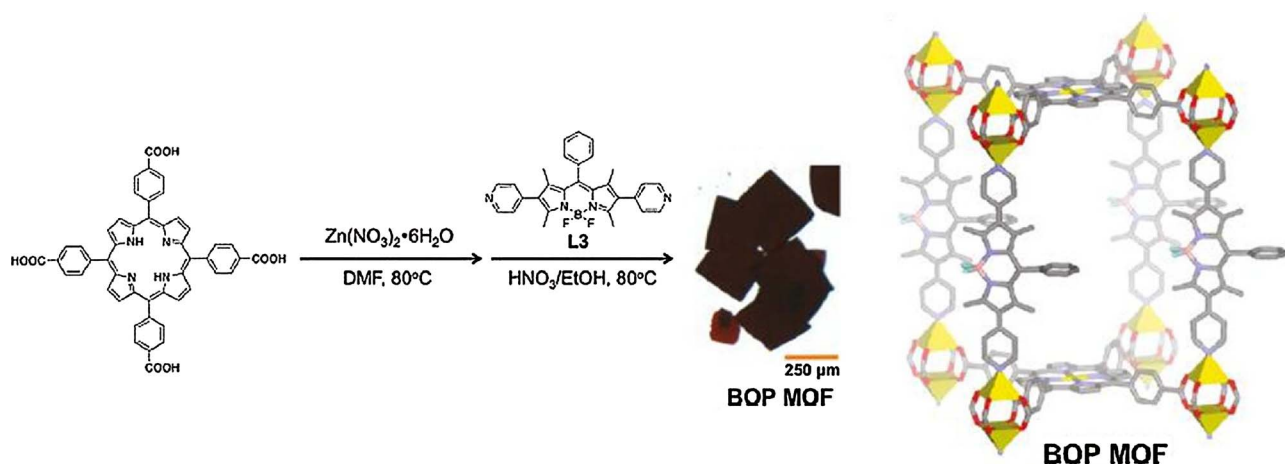


Fig. 4. Synthesis of the BOP MOF and its structure [67].

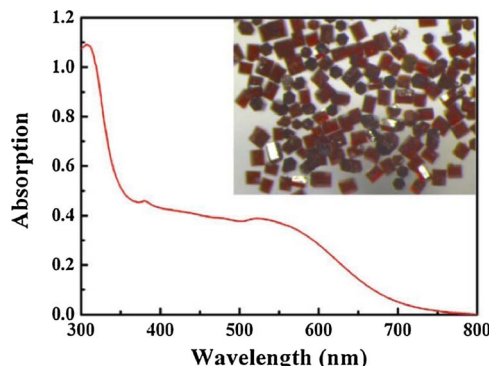


Fig. 5. UV-vis diffuse reflectance spectra of NTU-9 [40].

approaches: (1) Increase the absorption intensity to visible light, and (2) Reduce the recombination rate of the photo-induced electrons and holes. Toward this end, many different strategies have been reported, including decoration of linker or metal center, combination with semiconductors, metal nanoparticles (MNPs) loading, sensitization, pyrolyzation, decoration by GR or RGO and incorporation with functional materials. The modifications of MOFs, including UiOs (mainly UiO-66), MILs (mainly MIL-125, MIL-101, MIL-100 and MIL-53) and ZIFs (mainly ZIF-8 and ZIF-67), and their applications in photocatalysis will be introduced.

Table 1
Pristine MOFs for photocatalysts and their corresponding applications.

MOF species	Applications	Light source	Year	Ref.
$[\text{Co}_2(\text{C}_{10}\text{H}_8\text{N}_2)]_2[\text{C}_{12}\text{H}_8\text{O}(\text{COO})_2]_2$, $[\text{Ni}_2(\text{C}_{10}\text{H}_8\text{N}_2)]_2[\text{C}_{12}\text{H}_8\text{O}(\text{COO})_2]_2\text{H}_2\text{O}$	OG, RhB, RBBR and MB degradation	UV	2006	[53]
$[\text{Zn}_2(\text{C}_{10}\text{H}_8\text{N}_2)]_2[\text{C}_{12}\text{H}_8\text{O}(\text{COO})_2]_2$				
MOF-5	Phenol degradation	UV	2007, 2008	[39, 52, 55]
MOFs with changed linkers of MOF-5	Propylene oxidation	UV	2008	[54]
MIL-125	Alcohols oxidation, MB degradation	UV	2009, 2017	[59, 60]
UiO-66	H_2 production	UV	2010	[44]
ZIF-8	MB degradation	UV	2014	[58]
MIL-53(M) (M = Fe, Al, Cr)	MB degradation	UV-vis, visible	2011	[51]
UTSA-38	MO degradation	UV-vis	2011	[61]
BOB and BOP MOF	—	Visible	2011	[67]
Fe(III)-based MOFs	Rh6G degradation, O_2 production	Visible	2013, 2016	[68, 69]
NTU-9	RhB, MB degradation	Visible	2014	[40]
MOFs with changed linkers of UiO-66	MO degradation	Visible	2015	[57]
MIL-100, MIL-68	Benzene hydroxylation	Visible	2015	[65]
MIL-53(Fe)	$\text{Cr}(\text{VI})$ reduction, dyes degradation and water oxidation	Visible	2015, 2017	[62–64]
ZIF-67	$\text{Cr}(\text{VI})$ reduction	UV-vis-NIR	2016	[72, 73]
MIL-100(M) (M = Al, Fe, V, Cr)	MB degradation	UV	2016	[66]

300 to 440 nm. The amino substituent acts as an auxochromic and bathochromic group in the aromatic ring, leading to the absorption wavelength shift of UiO-66. The quantum yield for H₂ generation was 3.5% by UiO-66-NH₂ under monochromatic light at 370 nm in water/methanol 3:1. Although the quantum yield is still low, the amino decoration to UiO-66 opens a precedent for the subsequent linker decoration. In order to broaden the application scopes and explore the unfilled potential of UiO-66-NH₂, Wu and co-workers studied the photocatalytic selective oxidation of alcohols to their corresponding aldehydes and reduction of aqueous Cr(VI) utilizing UiO-66-NH₂ as the photocatalyst [78]. UiO-66-NH₂ exhibited photocatalytic activity in the two reactions under visible-light irradiation. To deepen the studies of the fundamental structure-property relations between the organic linker and the band gap of MOFs, Flage-Larsen and co-workers realized band gap modulations of the UiO-66-R (R = H, NH₂, NO₂) and the band gap changes could be quantified. They demonstrated that the NH₂ introducing reduced the band gap significantly and the changes not only related to the alters in the linker but also the nonbonding oxygen near the metalloid cluster [99]. Later, the band gap modulation by the same three linker designs (BDC, BDC-NO₂ and BDC-NH₂) of UiO-66 was investigated via the computation and experimental perspectives [100]. The reduced band gaps of UiO-66-NH₂ (2.75 eV) and UiO-66-NO₂ (2.93 eV) were highly influenced by the bonding nature between the functional group and the aromatic carbon ring, which was confirmed by the time-dependent density functional calculations. The above-mentioned two studies confirmed the linker decoration by NH₂ group for UiO-66 possesses the smallest band gap, which make the UiO-66-NH₂ a popular material for the various catalytic studies. Recently, a Zr-MOF-FePC decorated by 2-pyridinecarboxaldehyde (PC) and FeCl₃·6H₂O based on UiO-66-NH₂ was synthesized through combined covalent and dative post-synthetic modification [101]. The new multifunctionalized Zr-MOF can act as both a photocatalyst (Zr-oxo cluster), and a catalyst (Fe(III) in addition to Zr(IV) sites) for one-pot tandem photo-oxidative Passerini three-component reaction of alcohols.

Following this research direction, a series of mixed-linker Zr-based MOFs have been synthesized in one pot reactions for the visible-light photocatalytic oxidation of alcohol by Goh and co-workers [79]. The mixed-linker Zr-MOFs containing two linkers: (1) Primary linker: 2-amino-1,4-benzenedicarboxylate (NH₂-BDC) and (2) secondary linker: 2-X-1,4-benzenedicarboxylate (X-BDC, X = H, F, Cl, Br). Results revealed that the Zr-MOF containing mixed NH₂-BDC and F-BDC linkers performed five times more conversion compared to the Zr-MOF made of mixed NH₂-BDC and H-BDC linkers in the oxidation of benzyl alcohol. The enhanced photocatalytic activity was attributed to the partial substitution of the primary NH₂-BDC by electron-withdrawing halogenated BDC linkers. However, the effect of mixed linkers on the band gap of the Zr-MOFs was not researched comprehensively. To elucidate the effects of linker functional groups on the photoabsorption properties of UiO-66-X materials, a combined theoretical and experimental study were carried out by Hendrickx et al. [80]. The computed electronic properties of the periodic UiO-66 revealed that the band gap could be altered by linker functionalization and ranged from 4.0 to 2.2 eV (Fig. 6), suggesting the linker functionalization is indeed a promising way to modify the band gap of MOFs. They also proved that the bi-substituted linkers show smaller band gap energy than the mono-substituted linkers in the UiO-66.

The exchange of metal center of MOFs used to show no effect on the photocatalytic activity [51,52]. However, new findings suggested that partial substitution of metal center could influence the photocatalytic activity in a certain degree [77,82–84,102]. Metal doping becomes to be an effective way for enhancing the performance of semiconductor-based photocatalysts [103,104]. Constructing bimetallic assemblies by partial metal substitution brought out an enhanced photocatalytic performance particularly under visible light, because of the introduction of metal-to-metal charge transfer. The partial substitution of metal cations in MOFs can result in the formation of oxo-bridged hetero-

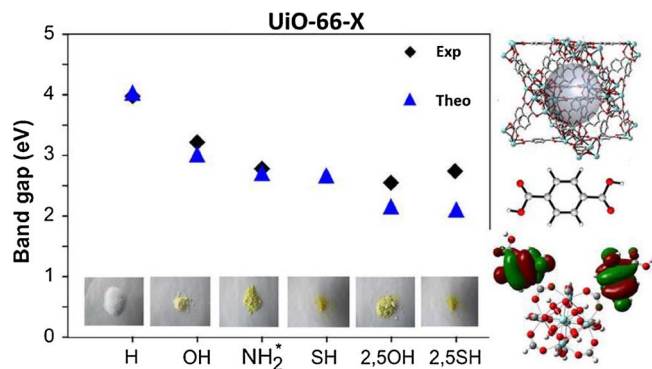


Fig. 6. The band gap of different linker-functionalized UiO-66 and its structure [80].

metallic assemblies within the same MOFs [105,106]. Such bimetallic assemblies, similar to those constructed over zeolites and semiconductors but with more flexibility and tenability owing to the availability of different structures of MOFs, are expected to show enhanced photocatalytic performance [82]. Li and co-workers demonstrated that the construction of the bimetallic assembly through the metal center substitution in MOFs was an efficient way to improve the photocatalytic activity of MOFs in 2014 [82]. They synthesized the Ti substituted UiO-66-NH₂ by a post-synthetic exchange (PSE) method and investigated its photocatalytic performance on the photocatalytic CO₂ reduction and H₂ production. The enhanced photocatalytic activity was due to that the introduced Ti substituent played a role of mediator to facilitate electron transfer according to the density functional theory (DFT) calculations and electron spin resonance (ESR) results. As shown in Fig. 7, the photo-excited electrons were produced when visible light irradiated on 2-aminoterephthalic acid (ATA) and then transferred to the Ti/Zr-O oxo-metal cluster (Ti/Zr)₆O₄(OH)₄ of Ti substituted UiO-66-NH₂. The photo-excited electrons were eager to transfer to Ti⁴⁺ rather than Zr⁴⁺ according to theoretical studies. Thus the intermediate (Ti³⁺/Zr⁴⁺)₆O₄(OH)₄ was formed and acted as an electron donor that donated electrons to Zr⁴⁺ to form Ti⁴⁺-O-Zr³⁺. As a result, the efficiency of interfacial charge transfer from ATA to Zr-O oxo-clusters was improved, leading to the enhanced photocatalytic activity. After that, the research group utilized the same method and prepared different amounts of Ti substituted UiO-66-NH₂ [83]. The transient absorption spectroscopy was studied systematically and a new application in photovoltaic cell was carried out. A perfect circle was provided and the Ti substituted UiO-66-NH₂ (NH₂-UiO-66(Zr/Ti)) reached a higher photon-to-current efficiency than UiO-66-NH₂.

Based on the above-mentioned work, more studies were carried out [77,84,102]. Lee introduced diamine-substituted ligands on the Ti substituted UiO-66-NH₂ via the PSE method (Fig. 8) for CO₂ reduction to HCOOH under visible-light irradiation [77]. Ti substitution decreased the electron accepting levels and the diamine-substituted ligands introduction offered new energy levels for additional light absorption and charge transfer, which is responsible for the enhanced photocatalytic activity. Yasin and co-workers demonstrated that the smallest band gap of partial Ti substituted UiO-66-NH₂ was UiO-66 (Ti₅Zr₁)-NH₂ (metal cluster: Ti₅Zr₁O₄(OH)₄) (2.60 eV) [102]. For the purpose of improving synthetic efficiency of Ti substituted UiO-66-NH₂, a microwave-assisted method was developed by Tu et al. [84]. The Ti substituted UiO-66-NH₂ could be prepared within a few hours rather than several days and the crystallinity well maintained. The prepared Ti substituted UiO-66-NH₂ showed enhanced photocatalytic activity for the photochemical vapor generation system to reduce Se(VI).

The decoration at molecular level (linker and metal center) to improve the photocatalytic activity of UiO-66 under visible-light is quite feasible. However, the choices of organic linkers modification and suitable substituted metal center are limited. Moreover, the separation efficiency of electrons and holes is incapable to be controlled. Other

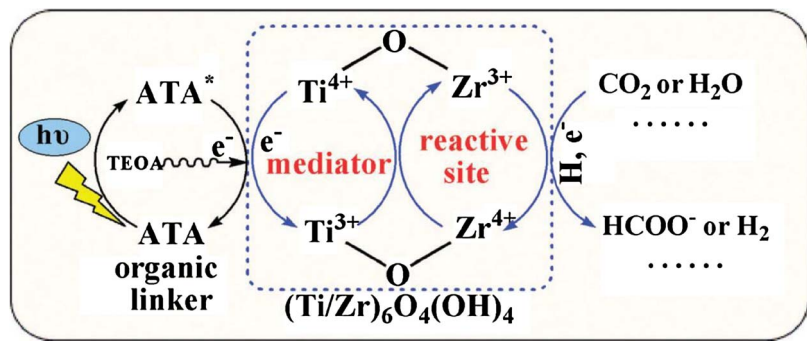


Fig. 7. Proposed enhanced mechanism for the photocatalytic reactions over Ti substituted UiO-66-NH_2 [82].

new strategies for improving the photocatalytic activity of UiO-66 are expected.

3.2. Combination with semiconductors

Compared to the method of linker or metal center decoration, an relatively ideal solution is to assemble UiO-66 with narrow band gap semiconductors to form heterogeneous photocatalysts [92]. There are two advantages: (1) the enlarged light absorption edge covering the visible-light area after the combination, leading to much narrower band gap compared to UiO-66 or UiO-66-NH_2 . (2) The enhanced separated efficiency of photo-induced electrons and holes due to the appearance of electron transfer between semiconductors and UiO-66 or UiO-66-NH_2 .

As a typical and important class of the II-VI semiconductor, CdS has been studied intensively and widely as practically applicable material in photocatalysis over the past decades owing to its narrow band gap (2.4 eV) as well as the size-dependent electronic and optical properties [107]. However, pure CdS particles have several issues that limit its utilization, including the aggregation of particles, high recombination rate of photogenerated electron-hole pairs and the property of photo-corrosion [108]. Therefore, anchoring CdS on MOFs is a promising choice to avoid the above mentioned problems. The CdS nanorods on UiO-66-NH_2 were realized by a facile room-temperature photodeposition and such nanocomposites behaved high photocatalytic activity for selective oxidation of alcohol (Fig. 9) [41]. The optical band gap of CdS-UiO-66(NH_2) and the amount of generated rodlike CdS could be tuned by changing the irradiation time during the CdS photodeposition. UiO-

66-NH_2 served not only as the support but also as the electrons provider to trigger the reaction for coupling itself with metal sulfides. Later, CdS was also loaded on UiO-66 by Zhou and co-workers through a hydrothermal process in 2015 [87]. The resulting CdS/UiO-66 hybrid composites exhibited remarkably active H_2 production under visible-light irradiation as compared to CdS and UiO-66 , which is ascribed to the effective separation of photo-induced electrons and holes across the composites.

Sheet-like structure materials, such as RGO and MoS_2 , incorporated on UiO-66/CdS could enhance the interfacial interaction between UiO-66 and CdS , leading to the improved charge transfer efficiency. Wu's group designed a ternary composite by introducing RGO to the UiO-66/CdS composite [85]. The introduction of RGO offers more efficient charge separation than that of binary system (UiO-66/CdS) according to the electrochemical impedance spectroscopy analysis. The prepared UiO-66/CdS/1%RGO performed a photocatalytic H_2 production rate 13.8 times as high as that of pure commercial CdS , and exhibited much higher photocatalytic efficiency than the inorganic semiconductor material — P25/CdS/1%RGO under visible light. The other ternary composite $\text{MoS}_2/\text{UiO-66/CdS}$ was also developed by Wu and co-workers [86]. MoS_2 as cocatalyst was deposited on UiO-66/CdS by a facile photo-assisted approach and the obtained composites possessed an intimate interfacial interaction among CdS , UiO-66 and MoS_2 . The H_2 production rate could reach $650 \mu\text{mol h}^{-1}$ when the content of UiO-66 was 50 wt% and MoS_2 was 1.5 wt%, which was nearly 60 times higher than that of pure CdS . $\text{Cd}_x\text{Zn}_{1-x}\text{S}$ solid solutions are promising materials because ZnS possesses the same coordination mode with CdS [109]. The band gap energy of the solid solution can be flexibly altered

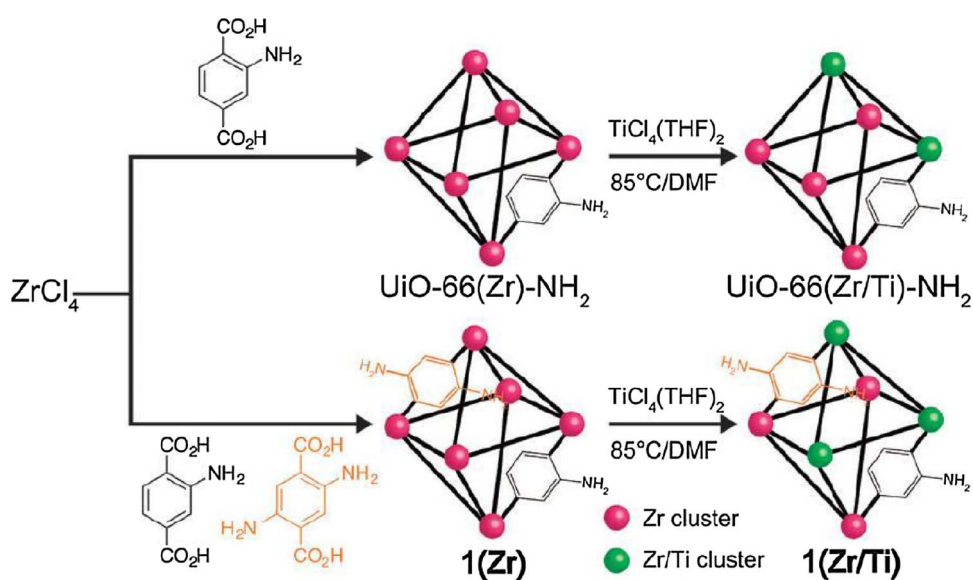


Fig. 8. Synthesis of mixed-ligand MOF 1(Zr) via PSE to obtain mixed metal MOFs 1(Zr/Ti), $\text{UiO-66(Zr/Ti)-NH}_2$ [77].

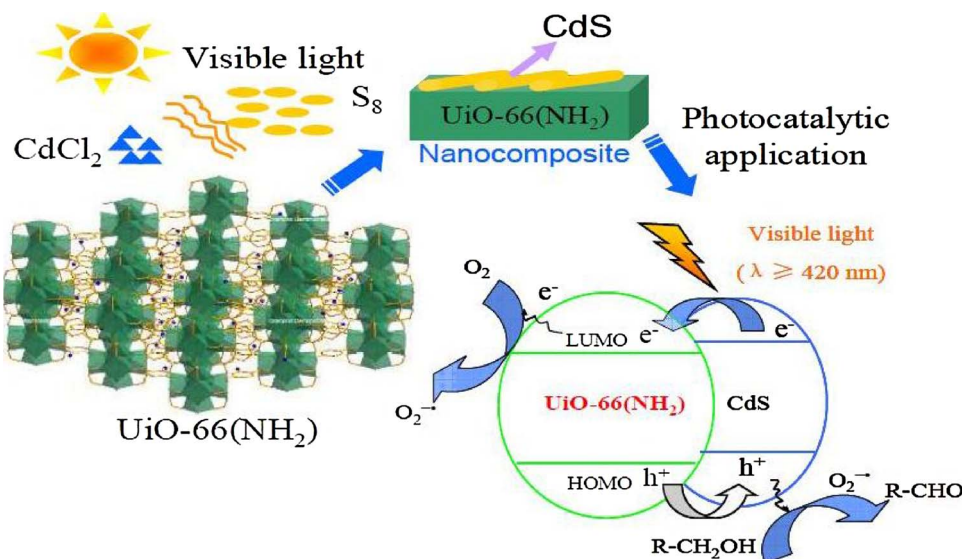


Fig. 9. The photodeposition of CdS on $\text{UiO-66}(\text{NH}_2)$ and its application for photocatalytic oxidation of alcohol [41].

by changing the molar ratio of CdS and ZnS [110]. Su and co-workers synthesized a highly active $\text{Cd}_{0.2}\text{Zn}_{0.8}\text{S}$ @ UiO-66-NH_2 composite photocatalysts by a facile solvothermal process for the H_2 production and CO_2 reduction under visible light. The H_2 and CH_3OH production rate could reach 5846.5 and $6.8 \mu\text{mol h}^{-1} \text{g}^{-1}$ respectively with 20 wt% content of UiO-66-NH_2 , which were much higher than that of $\text{Cd}_{0.2}\text{Zn}_{0.8}\text{S}$ and UiO-66-NH_2 . Inspired by their original work, our group chose ZIF-8 instead of UiO-66-NH_2 to load $\text{Cd}_{0.5}\text{Zn}_{0.5}\text{S}$ for the Cr(VI) photocatalytic reduction [111]. The existence of S-Zn bond between $\text{Cd}_{0.5}\text{Zn}_{0.5}\text{S}$ and ZIF-8 highly improved the photocatalytic activity and stability of $\text{Cd}_{0.5}\text{Zn}_{0.5}\text{S}$ @ZIF-8 composites.

Recently, bismuth-based semiconductors attracted extensive attention due to their narrow band gap energy (BiOBr : 2.8 eV, Bi_2MoO_6 : 2.6 eV) [91,93], great availability, non-toxicity and chemical inertness [112]. Three types of bismuth-based semiconductor: Bi_2WO_6 , BiOBr and Bi_2MoO_6 are combined with UiO-66 for the photocatalytic degradation of RhB under visible-light irradiation [89,91,93]. UiO-66 was incorporated with Bi_2WO_6 via a simple hydrothermal method by Sha and co-workers [89]. The active species involved in the degradation process were investigated by introducing different scavengers, and the results implied that $\cdot\text{O}_2^-$ and h^+ were two main active species in the photocatalytic degradation of RhB. $\text{Bi}_2\text{MoO}_6/\text{UiO-66}$ composites were synthesized via electrostatic interaction induced self-assembly process between Bi_2MoO_6 and UiO-66 by Ding and co-workers in 2017 [93]. These above mentioned bismuth-based-semiconductors incorporating with UiO-66 consistently demonstrated that the photo-induced $\cdot\text{O}_2^-$ and h^+ were the main active species in the photocatalytic degradation of RhB.

Other types semiconductor as outer antenna incorporating with UiO-66 have been extensively studied, such as, g-C₃N₄ [92], Ag_2CO_3 [90], AgI [113], CdSe [114], zinc phthalocyanine [94], MoS_2 [115], TiO_2 [116] and polyaniline [117]. Most of them possess a narrow band gap that could absorb visible light abundantly, and UiO-66 or UiO-66-NH_2 not only acts as a perfect substrate, but also a semiconductor to accept or transfer the photo-induced electrons. Thus the separation efficiency of electron-hole pairs will be improved, leading to an enhanced photocatalytic activity. Graphitic carbon nitride, a stable, metal-free and visible-light active photocatalyst, has attracted intensive attention as photocatalysts in different fields [118,119]. In 2015, Shi and co-workers prepared a UiO-66/CNNS (carbon nitride nanosheet) hybrid structure by electrostatic self-assembly of negatively charged CNNS with positively charged UiO-66 [92]. This is the first time that a MOF/CNNS hybrid structure was prepared by electrostatic self-

assembly. They demonstrated that the photo-excited electrons could transfer from CNNS to UiO-66 in UiO-66/CNNS , leading to a much higher photocatalytic activity for the CO_2 conversion than that of bare CNNS. To improve the photocatalytic activity and stability of pristine Ag_2CO_3 , UiO-66 was incorporated with Ag_2CO_3 via a convenient solution method by Sha and co-workers [90]. The prepared $\text{Ag}_2\text{CO}_3/\text{UiO-66}$ showed enhanced photocatalytic activity for RhB degradation compared to the physical mixture of UiO-66 and Ag_2CO_3 under visible-light illumination. This was ascribed to more Ag_2CO_3 active sites on the composite surface. By virtue of the advantages of metal center partial substitution of UiO-66 , Xu and co-workers incorporated polyaniline (PANI) with Fe UiO-66 (iron doped UiO-66) by annealing process [117]. The photocatalytic performance were evaluated by the selectively oxidation of various alcohol under visible-light irradiation using molecular oxygen as a benign oxidant. The superior photocatalytic activity of PANI/Fe UiO-66 nanohybrids was ascribed to valence fluctuation of $\text{Fe}^{2+}/\text{Fe}^{3+}$ and formed heterostructures between PANI and UiO-66 , which could enhance the separation efficiency of photogenerated carriers. Moreover, the major contributors to the oxidation of alcohols were $\cdot\text{O}_2^-$ and h^+ , which was proved as well. Combination with semiconductors is the most commonly used strategies to modify MOFs for photocatalysis, but seeking a very ideal semiconductor for greatly improving the activity and practicability is still a big challenge.

3.3. MNPs loading

MNPs attracted enormous attention in the past decade because of their great potential in different kinds of applications, especially in catalysis [120]. Size shrinkage of the particles to nanoscale can significantly enhance their catalytic efficiency due to the high surface-to-volume ratio, great ratio of atoms remaining at the large surface area, and the high density of the coordination unsaturated sites [121]. As for photocatalytic reactions, metal loading scarcely improves the absorption of visible light, which means that the little red-shift for the materials is derived from the color change [96]. Metals of Au, Ag, and Cu could increase the light absorption via the localized surface plasmon resonance (LSPR) under visible-light irradiation. Pd NPs of about 3–6 nm in diameter were highly dispersed and immobilized in UiO-66-NH_2 via a facile one-pot hydrothermal method by Wu's research group [95]. Due to the high dispersion of Pd NPs and their close contact with UiO-66-NH_2 , the resulting Pd@ UiO-66-NH_2 was utilized as a highly efficient bifunctional photocatalyst to remove Cr(VI) and dyes simultaneously. Cr(VI) reduction by electrons (e^-) and dyes oxidation by

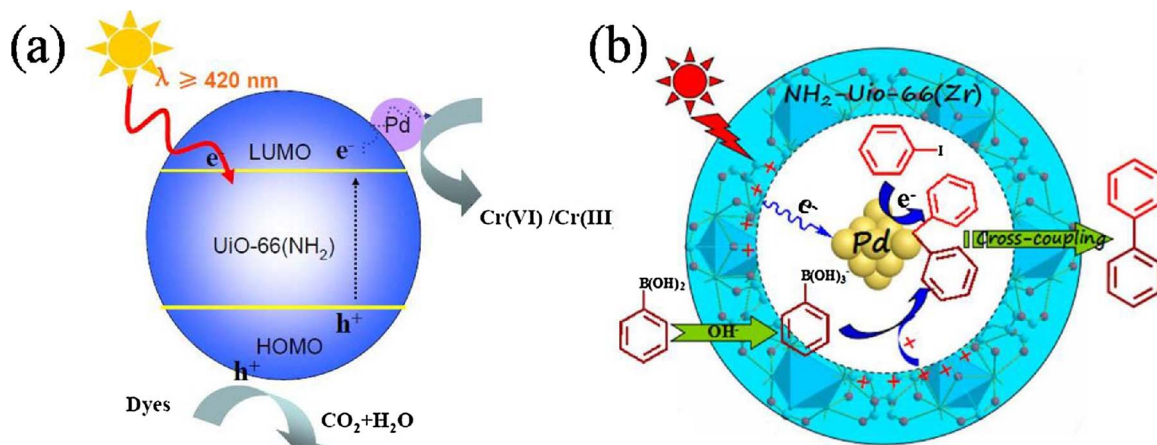


Fig. 10. Proposed mechanism of the visible-light catalytic remove of Cr(VI) and dyes [95] (a) and Suzuki Coupling Reaction over $\text{Pd}@\text{UiO-66-NH}_2$ [96] (b).

holes (h^+) occurred in the both ends of LUMO and HOMO in $\text{UiO-66}(\text{NH}_2)$ (Fig. 10a), which highly promoted the two reactions simultaneously. The Pd NPs accepted the photo-excited electrons from UiO-66-NH_2 to reduce Cr(VI). Later, smaller Pd nanoclusters ($< 1.2 \text{ nm}$) were encapsulated inside the cage of UiO-66-NH_2 via a double-solvent approach followed with a photoreduction process [96]. The resulting $\text{Pd}@\text{UiO-66-NH}_2$ performed efficiently in the visible-light-promoted Suzuki coupling reaction (Fig. 10b). Two factors contributed to the significantly enhanced photocatalytic activity, one is the presence of abundant coordinated unsaturated active Pd sites, the other is the efficient photo-excited electrons transfer from UiO-66-NH_2 to the confined Pd nanoclusters.

Up to now, research into MNPs loading on the UiO-66 for photocatalysis is rare. Because the MNPs (except Au, Ag and Cu) loading can not increase the visible-light absorption. They majorly served as electron acceptor and mediator and the substrate need to absorb visible light. Thus the substrate is always based on visible-light responsive MOFs, such as UiO-66-NH_2 .

3.4. Sensitization

Since the first study of dye-sensitized colloidal TiO_2 films with an enhanced light-to-electric energy conversion yield in 1991 [122], dye-sensitization has become a relatively mature technology for the red shift of semiconductor photocatalysts to enhance the visible-light harvesting. In addition, given both partial MOFs (the organic linker contains benzene ring, e.g. UiO-66 and MIL-125) and dyes containing benzene ring, it is expected that a strong $\pi-\pi$ stacking and Van Der Waals interaction formation between MOFs and dyes, which is significant for the efficient charge transfer in a dye-sensitized photocatalyst system. Thus, MOFs decorated by dye sensitization as photocatalysts are accessible and feasible. He and co-workers reported that $\text{Pt}@\text{UiO-66}$ sensitized by adsorbed or directly added RhB dye showed enhanced photocatalytic activity for H_2 production under visible-light illumination in 2014 [42]. The absorption intensity of $\text{Pt}@\text{UiO-66}$ in the visible-light region was significantly improved after RhB sensitization, the spectra in 450–600 nm was similar to that of RhB, and RhB absorbed the light and transformed into RhB^+ . Meanwhile, the photo-excited electrons transferred to the LUMO of UiO-66 and then a series of reaction happened (Fig. 11). The adsorbed and directly added RhB dye sensitized $\text{Pt}@\text{UiO-66}$ extremely enhanced the photocatalytic efficiency to 30 and 26 times as high as that of bare $\text{Pt}@\text{UiO-66}$, respectively. Limited for the poor photostability of RhB [123], the low cost Erythrosin B (ErB) dye sensitized UiO-66 has been prepared by Yuan and co-workers for photocatalytic H_2 production under visible-light irradiation [43]. The highest H_2 production rate was $4.6 \mu\text{mol h}^{-1}$ which occurred from the system containing 10 mg of MOFs photocatalyst and 30 mg ErB with the Pt as a

cocatalyst. The dye sensitized UiO-66-NH_2 was also carried out using a diazo-coupling reaction by Otal and co-workers [97] in 2016. The diazo-coupling reactions of UiO-66-NH_2 with naphthols and aniline yielded reddish samples, and diphenylaniline yielded dark violet ones, resulting in a huge red-shift of the optical absorption of UiO-66-NH_2 [97]. The expanded absorption edge of dye sensitized UiO-66-NH_2 confers the higher photocatalytic activity than that of traditional TiO_2 for the degradation of MB.

Given the low cost and easy operation of dye sensitization to MOFs, these studies provide a potential approach to developing highly efficient and practical MOF-based photocatalysts for hydrogen production and environmental remediation. However, it is noticed that the stability of dyes is very important, or else it will bring secondary pollution.

3.5. Decoration by RGO

Reduced graphene oxide (RGO) has been considered as an ideal component for fabricating various functional composite materials because of its superior physicochemical properties [124]. In addition, RGO can act as an electron sink to accept the photo-excited electrons from semiconductor that will inhibit the recombination of electrons and holes. However, similar to the MNPs loading, combination with RGO can not increase the visible-light absorption [4,98]. Thus, the RGO decoration is depending on the substrate that could absorb visible light, and UiO-66-NH_2 is the common choice as well. Wu and co-workers assembled RGO/ UiO-66-NH_2 nanocomposites by an electrostatically derived self-assembly of the positively charged UiO-66-NH_2 and the negatively charged GO in water [4]. After a hydrothermal reduction process, the obtained RGO/ UiO-66-NH_2 nanocomposites showed significantly enhanced visible-light photocatalytic activity for Cr(VI) reduction. In order to fully utilize the superiority of the two-dimensional sheet structure of RGO, a layered sandwich-like hierarchical nanoarchitecture of photoactive RGO/ UiO-66-NH_2 was fabricated via a noncovalent methodology for graphene functionalization and a solvothermal synthesis (Fig. 12a) [98]. The pyrene⁺, an amphiphilic pyrene derivative, acted as stabilizer and connector between RGO and UiO-66-NH_2 , leading to an intimate contact between them. The unique sandwich-like heterostructure could promote the separation and transfer of photo-excited charges, leading to the enhanced photocatalytic activity for the selective photocatalytic oxidation of benzyl alcohol under visible-light irradiation (Fig. 12b).

UiO-66 is the most typical and popular MOFs utilized until today due to its excellent photocatalytic properties. Although, the independent research of linker or metal center decoration, combination with semiconductors, MNPs loading, sensitization and decoration by RGO are tremendous, the cross-over studies among these modified methods are likely to be the major direct for the further investigation of

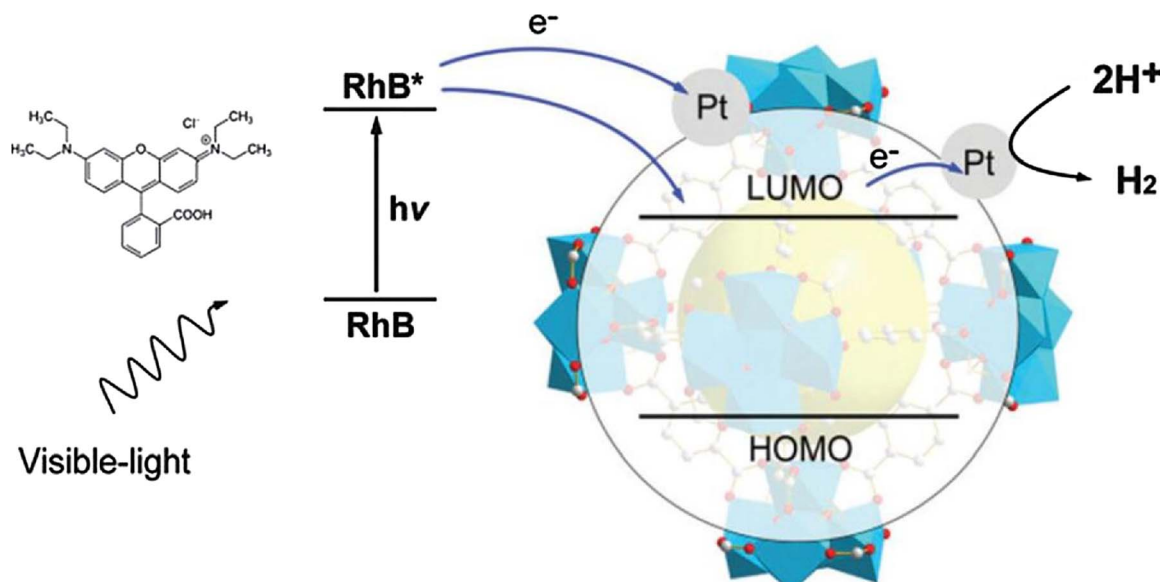


Fig. 11. Proposed mechanism of photocatalytic H_2 production over RhB-sensitized Pt@UiO-66 under visible-light irradiation [42].

UiO-66 and the brilliant designs of ternary or multi-system are expected. The modified strategies of UiO-66 and their corresponding applications are listed in Table 2.

4. MILs

MILs including MIL-125, MIL-101, MIL-100 and MIL-53 have been widely applied in photocatalysis. Among them pristine MIL-125 is responsive to UV-light irradiation, whereas pristine MIL-101, MIL-100 and MIL-53 are visible-light responsive MOFs.

4.1. Ti-based MIL-125

Titanium is a very attractive candidate element for the design of photocatalysts due to its low toxicity, redox activity and photocatalytic properties. MIL-125 ($Ti_3O_8(OH)_4(BDC)_6$, MIL = Materials of Institut Lavoisier) constructed from titanium-oxo-hydroxo clusters and H_2BDC linkers was synthesized in 2009 [59]. MIL-125 is thermally robust up to 360 °C, which is fundamental for the design of photocatalysts under a certain temperature. However, similar to UiO-66, MIL-125 possesses a wide band gap energy of 3.6 eV [125], suggesting that the MIL-125 can be merely excited by UV-light irradiation and the separation efficiency of photo-induced charge carriers is low. Thus, the modification to MIL-

125 as photocatalysts is necessary.

4.1.1. Decoration of linker

Decoration of a linker and partial substitution of metal centers are two typical ways of UiO-66 decorated at the molecule level. However, as for MIL-125, there is merely linker decoration to enhance its photocatalytic activity, no report about the metal center partial substitution, and it is probably because the metal center Ti of MIL-125 is an excellent catalytic sites and substitution of other metal is likely to decrease the catalytic activity. In the studies of linker decoration of MIL-125, the introduction of NH_2 groups in BDC linker still played the major role. MIL-125 shows an absorption edge to 350 nm corresponding to the absorption of Ti-O oxo-clusters. MIL-125- NH_2 shows an extra absorption band in the visible-light region with the absorption edge around 550 nm, which is ascribed to the ligand-based absorption. The visible-light absorption is ascribed to the conjugated π electron transition from the amine containing chromophores to the Ti-oxo clusters. Li and co-workers firstly utilized MIL-125- NH_2 for the photocatalytic reduction of CO_2 to $HCOO^-$ under visible-light irradiation in 2012 [45]. Although the efficiency of the reduction of CO_2 over MIL-125- NH_2 photocatalyst was low, this work signified that MOFs as photocatalysts hold great promise for the reduction of CO_2 . Later on, they used MIL-125- NH_2 for the aerobic selective oxidation of amines to imines under visible-light

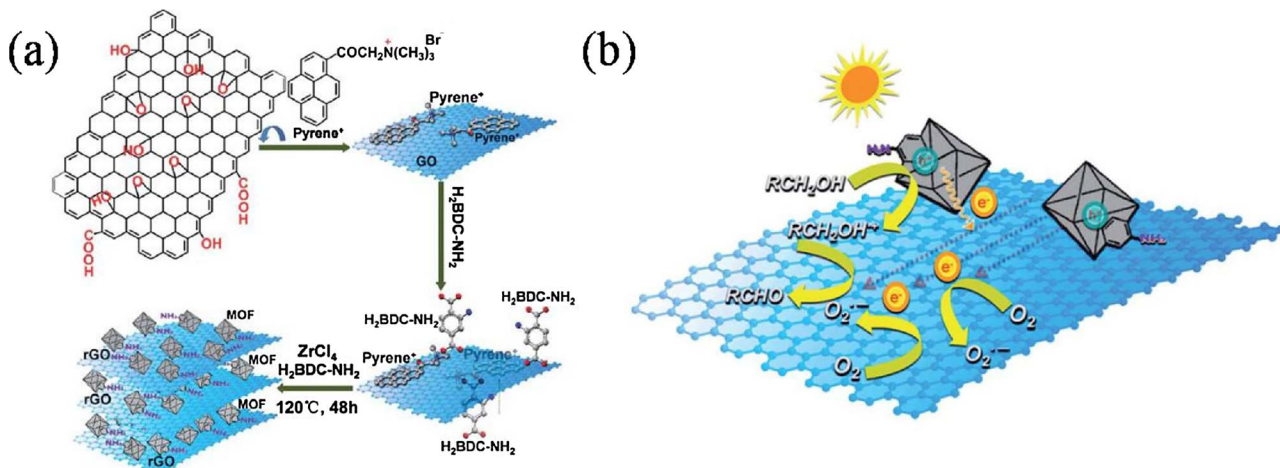
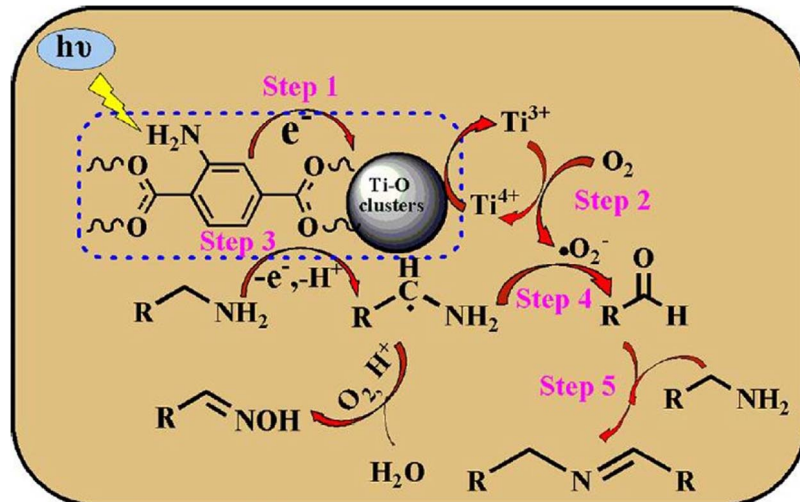


Fig. 12. Fabrication procedures of the layered RGO/UiO-66-NH₂ hybrids (a) and proposed mechanism for the enhanced photocatalytic oxidation over RGO/UiO-66-NH₂ hybrids (b) [98].

Table 2

Modified strategies of UiO-66 and their corresponding applications.

Strategies	details	MOF	Applications	Light source	Ref.
Combination with semiconductors	-NH ₂	UiO-66	H ₂ production	UV	[44]
	-NH ₂	UiO-66	Alcohol oxidation, Cr(VI) reduction	Visible	[78]
	-F, Cl, Br	UiO-66	Alcohols oxidation	Visible	[79]
	-NH ₂ , NO ₂ , Br	UiO-66	Cr(VI) reduction	UV-vis	[81]
	Ti substitution	UiO-66-NH ₂	Cr(VI), CO ₂ reduction, cell.	Visible	[77,82,83]
	Ti substitution	UiO-66	Se(VI) reduction	UV	[84]
	CdS	UiO-66-NH ₂	Alcohols oxidation	Visible	[41]
	CdS	UiO-66	H ₂ production	Visible	[87]
	CdS	GO/UiO-66	H ₂ production	Visible	[85]
	MoS ₂ /CdS	UiO-66	H ₂ production	Visible	[86]
MNPs loading	Cd _{0.5} Zn _{0.5} S	UiO-66-NH ₂	CO ₂ reduction and H ₂ production	Visible	[88]
	CdSe	UiO-66	RhB degradation	Visible	[114]
	Bi ₂ WO ₆	UiO-66	RhB degradation	Visible	[89]
	BiOBr	UiO-66	RhB degradation	Visible	[91]
	Bi ₂ MoO ₆	UiO-66	RhB degradation	Visible	[93]
	AgCO ₃	UiO-66	RhB degradation	Visible	[90]
	g-C ₃ N ₄	UiO-66	CO ₂ reduction	Visible	[92]
	AgI	UiO-66	RhB degradation	Visible	[113]
	TiO ₂	UiO-66-NH ₂	CO ₂ reduction	UV-vis	[116]
	MoS ₂	GO/UiO-66-NH ₂	H ₂ production	Visible	[115]
Sensitization	ZnTCPc	UiO-66-NH ₂	MB degradation	Visible	[94]
	PANI	FeUiO-66	Alcohols oxidation	Visible	[117]
Decoration by RGO	Pd	UiO-66-NH ₂	Cr(VI) reduction, dyes degradation	Visible	[95]
	Pd	UiO-66-NH ₂	Suzuki coupling reaction	Visible	[96]
Decoration by RGO	RhB	Pt/UiO-66	H ₂ production	Visible	[42]
	ErB	Pt/UiO-66	H ₂ production	Visible	[43]
Decoration by RGO	Naphthols, aniline and diphenylaniline	UiO-66-NH ₂	MB degradation	UV-vis	[97]
	RGO	UiO-66-NH ₂	Cr(VI) reduction	Visible	[4]
	RGO	UiO-66-NH ₂	Alcohols oxidation	Visible	[98]

Fig. 13. The proposed photocatalytic process of the photocatalytic amines oxidation over MIL-125-NH₂ [126].

irradiation and the proposed photocatalytic process was showed in Fig. 13, which clearly exhibited the transfer route of photo-excited electrons [126]. Very recently, in order to deeply study the relationship between the catalytic performances and the amount of functionalized linkers of MIL-125-NH₂, Chambers and co-workers assessed the photocatalytic activity for the oxidation of benzyl alcohol to benzaldehyde with the increasing amounts of BDC-NH₂ linkers (0%, 20%, 46%, 70% and 100%) incorporated in the framework [127]. Results demonstrated the maximum photocatalytic activity was ~50% BDC-NH₂ content incorporating into the framework, which was ascribed to the occurrence of the mixed valence Ti⁴⁺-Ti³⁺ state within the Ti₈-wheels in crystal structure of MIL-125. The two studies both verified the switch between Ti⁴⁺ and Ti³⁺ of MIL-125-NH₂ in the photocatalytic process. The spectroelectrochemistry and ultrafast spectroscopy have proved that the electron is located in the Ti-oxo clusters and the hole resides in the

amino terephthalate unit particularly the amino group upon photo-excitation [128], which further improved the route of electron transfer in the photo-excited MIL-125-NH₂. The other photocatalytic applications utilizing MIL-125-NH₂ as catalyst were also been reported, such as the photocatalytic reduction of Cr(VI) [129], photoredox synthesis of N-hydroxy-oxazolidinones [130] and photochemical vapor generation (PCVG) for determination of selenium [131].

Hendon and co-workers explored the diaminated linker BDC-(NH₂)₂ and other functional groups (-OH, -CH₃, -Cl) as alternative substitutes to control the optical response in silico [125]. Weaker electron-donating substitutions reduced the band gap to a lesser extent, e.g. -CH₃. However, stronger electron-donating substitutions such as amines significantly reduced the band gap. Results demonstrated -NH₂, -OH, -CH₃ and -Cl are the most promising and favorable substitutions. In addition, the diaminated BDC-(NH₂)₂ linker exhibited

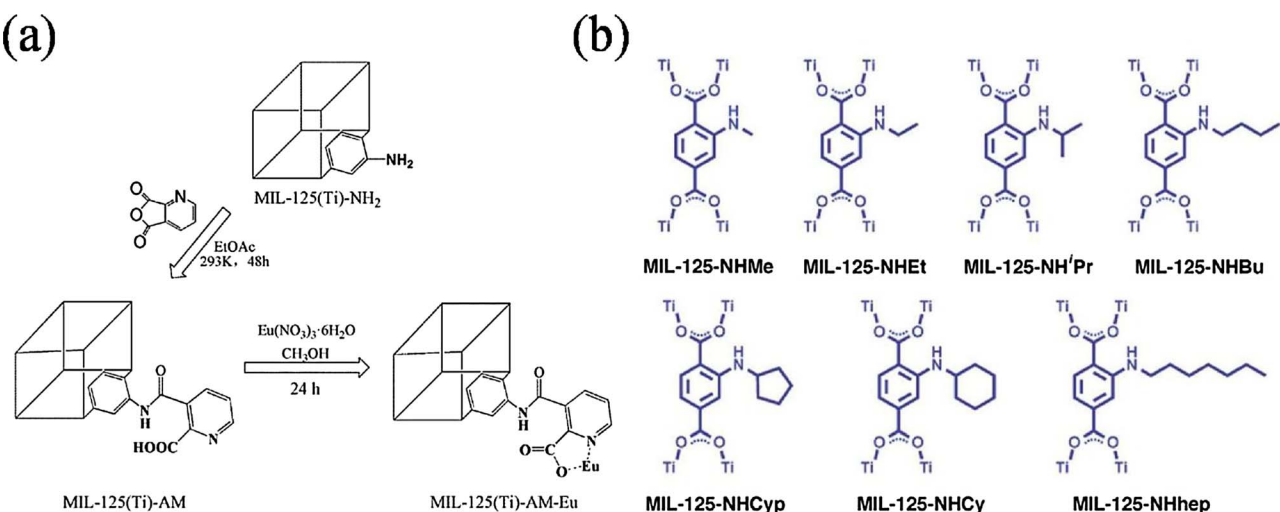


Fig. 14. Synthesis procedure of MIL-125-AM-Eu [132] (a) and N-alkyl substituted isoreticular MOFs based on MIL-125-NH₂ [133] (b).

the most significant red shift of 1.3 eV/950 nm with the synthesis of 10%-MIL-125-(NH₂)₂/90%-MIL-125-NH₂. A new Europium functionalized material based on MIL-125-NH₂ was prepared by covalent post-synthetic modification and Eu³⁺ coordinate load (Fig. 14a) [132]. The manufactured material performed high conversion and selectivity for photocatalytic oxidation of α -phenethyl alcohol. Recently, a series of MOFs isoreticular to MIL-125-NH₂ were synthesized by increasing the N-alkyl substitution in MIL-125-NHR, where R varies from methyl (Me) to ethyl (Et), isopropyl (*i*Pr), n-butyl (Bu), cyclopentyl (Cyp), cyclohexyl (Cy), and *n*-heptyl (hep) (Fig. 14b) [133]. The prepared materials showed a gradual decrease in the optical band gap from 2.56 eV of MIL-125-NH₂ to 2.29 eV of MIL-125-NHCy, which was consistent with the increased electron density around the organic linker via inductive effects of the N-alkyl chain and the increased reaction rates and quantum yields for the photocatalytic reduction of carbon dioxide under blue LED light. In particular, MIL-125-NHCy had a smaller band gap (E_g = 2.3 eV), a longer-lived excited-state (τ = 68.8 ns) and a larger apparent quantum yield (ϕ_{app} = 1.8%) than that of pristine MIL-125-NH₂ (E_g = 2.56 eV, τ = 12.8 ns, ϕ_{app} = 0.31%). The morphologies and sizes modification of MIL-125-NH₂ crystal utilizing a facile surfactant for photocatalysis also has been studied. The surfactants of Pluronic P123 [134] and cetyltrimethyl ammonium bromide [135] were investigated and the modified MIL-125-NH₂ showed enhanced photocatalytic activity for the deoxygenation reaction [134] and RhB degradation [135].

4.1.2. Combination with semiconductors

For MIL-125, the strategy by combining with semiconductor for photocatalysis is also frequently-used. The mechanism is the same as that of UiO-66. Highly photoactive g-C₃N₄/MIL-125 hybrids with large surface area, mesoporous heterostructures and stability were synthesized by a solvothermal strategy and the bulk g-C₃N₄ acted as the supporter for the formation of heterostructures (Fig. 15a) [136]. The composites showed more efficient photocatalytic performance for RhB degradation that is 2.1 and 24 times as high as that of pure g-C₃N₄ and MIL-125. The indirect dye photosensitization, Ti³⁺-Ti⁴⁺ intervalence electron transfer and the synergistic effect between MIL-125 and g-C₃N₄ were responsible for the enhanced photocatalytic activity. However, bulk g-C₃N₄ suffers the predicament of limited photocatalytic activity due to low quantum yield and high recombination rate of photo-induced charge carriers [136]. The layer g-C₃N₄ nanosheets with high specific surface area exhibit many intriguing properties compared to bulk g-C₃N₄ [137]. On this basis, a new hybrid heterostructured MIL-125/Ag combined with g-C₃N₄ nanosheets were prepared by Yang and co-workers in 2017 [138]. During the process, MIL-125/Ag was firstly

synthesized by a photo-reduction deposition method and then g-C₃N₄ nanosheets were adhered onto the MIL-125/Ag composite. Ag NPs acted as an electron-conduction bridge in the interface between MIL-125 and g-C₃N₄ nanosheets, which facilitate the direct migration of photo-induced electrons from g-C₃N₄ to MIL-125 and retard the recombination of electron-holes. The MIL-125/Ag/g-C₃N₄ nanocomposites showed high photocatalytic activity both for the photocatalytic reduction of nitrocompounds and the oxidation of alcohols. A latest study developed MIL-125-NH₂/g-C₃N₄/NiPd composites by coating g-C₃N₄ nanosheets on MIL-125-NH₂ and followed by depositing Ni/Pd co-catalysts onto MIL-125-NH₂/g-C₃N₄ surface [139]. Compared to the monometallic-based photocatalysts, MIL-125-NH₂/g-C₃N₄/Ni_{15.8}Pd_{2.1} behaved the highest photocatalytic activity for H₂ production rate of 8.7 mmol g⁻¹ h⁻¹. Very recently, the Z-scheme heterojunction photocatalysts captured plenty of attention [140], owing to the high charge separation efficiency and strong redox ability. However, the construction of Z-scheme heterojunction photocatalysts based on MOFs was infrequent. Zhou and co-workers firstly combined the MIL-125-NH₂ with g-C₃N₄ functionalized by benzoic acid to synthesize the g-C₃N₄/MIL-125-NH₂ Z-scheme heterostructured photocatalysts for the H₂ production (Fig. 15b) [141]. Benzoic acid functionalized g-C₃N₄ participated in the coordination of Ti₈O₈ clusters and 2-aminoterephthalic acid, and g-C₃N₄ finally connected with MIL-125-NH₂ by covalent bonds. The bond acted as a mediator for the transfer of electrons from the conduction band of g-C₃N₄ to the value band of MIL-125-NH₂ and meanwhile combined with the holes on MIL-125-NH₂, leading to a strong redox ability.

Many other semiconductors combination with MIL-125 have been reported as well. In 2014, MIL-125@TiO₂ composite was synthesized by a single-step hydrothermal synthesis for the application of a depleted perovskite/TiO₂-MOF heterojunction solar cell [142]. Later, a MIL-125-NH₂/TiO₂ hybrid was synthesized to construct a sensitive photoelectrochemical sensor for the determination of the herbicide clethodim under visible-light irradiation [143]. In 2016, a novel core-shell In₃S₃@MIL-125 composite that MIL-125 acted as the core and three-dimensional In₃S₃ sheets network as the shell was prepared via a facile solvothermal method for the photocatalytic degradation of tetracycline [144]. At the same year, a series of BiOBr/MIL-125-NH₂ composites were prepared by a co-precipitation method and the prepared composites showed an enhanced photocatalytic activity for the degradation of RhB [145]. Very recently, a potassium poly (heptazine imide) (PHIK) were incorporated into MIL-125-NH₂ via simply dispersing the two materials in water in virtue of the electrostatic interactions [146]. The PHIK possesses negative surface charge while MIL-125-NH₂ takes positive surface charge. The composites exhibited a superior

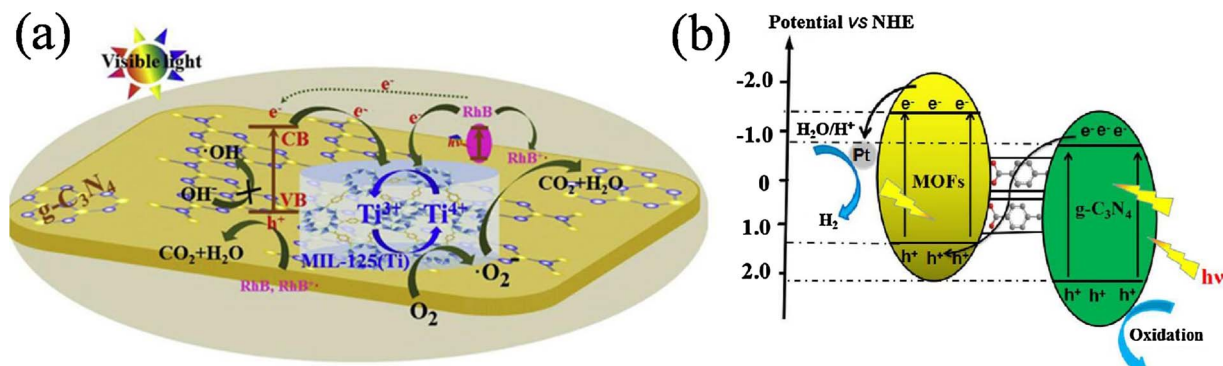


Fig. 15. The photocatalytic degradation procedure of RhB over g-C₃N₄/MIL-125 hybrid [136] (a) and the H₂ production through the Z-scheme heterostructured photocatalyst [141] (b).

photocatalytic activity in RhB degradation under blue light irradiation (465 nm).

4.1.3. MNPs loading

The studies for MNPs loading on MIL-125 as photocatalyst are more than those of UiO-66 and the investigations mainly focus on Pt [147–150], Au [148,149], Pd [149], Ag [151–153] and Ni [154,155]. The first attempt for Pt NPs loading on MIL-125-NH₂ was for hydrogen production in 2012 [150]. The transferred routes of photo-induced electrons among organic linker, titanium-oxo cluster and Pt NPs have been investigated in detail. Later, Pt@MIL-125-NH₂ has been applied as a photocathode material for photoelectrochemical hydrogen production [147]. The Pt@MIL-125-NH₂ was successfully synthesized by a double solvents method, and the internal Pt NPs were smaller than 4 nm. Li and co-workers synthesized M/MIL-125-NH₂ (M = Pt and Au) via a wetness impregnation method followed by a treatment with H₂ flow [148]. Its photocatalytic activities were evaluated by the photocatalytic reduction of CO₂ to formate. Compared with pristine MIL-125-NH₂, Pt and Au loading exhibited different effects on the photocatalytic performance, where Pt/MIL-125-NH₂ showed an enhanced activity for photocatalytic formate formation while Au had a negative effect on the reaction. The ESR studies and DFT calculations demonstrated that the hydrogen can spillover from Pt to the bridging oxygen linked to Ti atoms, resulting in the formation of Ti³⁺ and an enhanced performance for CO₂ reduction to produce formate. However, the behavior was difficult for Au/MIL-125-NH₂ to achieve, leading to a poor photocatalytic performance. In the preparation of MNPs/MOFs, the strong reducing and capping agents are necessary to control the morphology and size distribution of metal NPs. However, the residual organic agents are detrimental to the catalytic reaction. Thus, a facile and general method without using extra reducing and capping agents is necessary. In 2015, through a redox reaction between the reductive MIL-125 with Ti³⁺ and metal salt precursors, Pt, Au and Pd NPs were uniformly deposited onto MIL-125 without using any extra reducing or stabilizing agents (Fig. 16) [149]. The prepared M/MIL-125 (M = Pt, Au and Pd) showed enhanced photocatalytic activity for the selective oxidation of benzyl alcohol and H₂ production compared to pure MIL-125.

Ag NPs are known as good electron sinks due to the Schottky barrier at the metal-semiconductor interface [156]. Via post-synthetic modification of MIL-125-NH₂ with acetylacetone (AC) vapor under nitrogen followed by the reduction of Ag⁺, Ag/MIL-125-AC had a band gap of 2.09 eV and a remarkably improved photocatalytic activity for the degradation of MB under visible-light irradiation [151]. Simultaneously, Ag/MIL-125 composites with a uniform diameter of about 40 nm of Ag NPs have been prepared by a hydrothermal and photo-reduction method in 2015 [153]. GO decorated Ag/MIL-125 were also synthesized via one-pot self-assembly and photoreduction strategy [152]. The two composites were utilized for the photocatalytic degradation of RhB under visible-light irradiation. A composite of MIL-125-NH₂ and a molecular [Ni(dmobpy)(2-mpy)₂] catalyst has been prepared by

stepwise assembly of the complex in the presence of a MOF [155]. The resultant composite was evaluated by photocatalytic hydrogen production. Over the course of the composite catalyst's lifetime, different nickel (Ni) species played the leading roles and Ni²⁺ was reduced into catalytically active elemental nickel with the first efficient 1000 min. In addition, the Ni NPs-doped MIL-125-NH₂ was also developed for the photocatalytic aerobic oxidation of aromatic alcohols under visible-light irradiation by Fu and co-workers [154].

4.1.4. Pyrolyzation

The synthesis and characterization of transition metal oxides with controlled size and shape as well as uniform dimension have drawn intensive interests due to their unique physical and chemical properties and promising applications in the fields of catalysis [157–159]. Among them, titania (TiO₂) is a typical and practical photocatalyst due to its unique properties, economy and nontoxicity [160–162]. Nevertheless, the syntheses of TiO₂ with controlled phase, shape and morphology still remain a challenge. MOFs possess highly ordered porous structures with abundant organic ligands and its metal and oxygen atoms arrange at the periodical atom level in MOFs crystals. Thus, MOFs can be completely converted into metal oxides without long-range atomic migration, which would be good candidates as sacrificial templates to give highly porous carbon or oxide materials under proper thermolysis conditions [163]. Therefore, TiO₂ derived from pyrolysis of MIL-125 for photocatalysis is a typical example, though most of photocatalytic reactions were carried out under UV-light irradiation.

In 2014, a series of TiO_x/C composites were prepared by pyrolyzing MIL-125 under Ar atmosphere at 400, 600, 800 and 1000 °C, respectively [164]. Its photocatalytic performance was evaluated by the degradation of MB, and the best photocatalytic performance was achieved in MIL-125 pyrolyzed at 1000 °C due to its high surface area, reduced Ti₃O₅ composition and conductive matrix. TiO₂ derived from MIL-125 pyrolysis could act as a support matrix for the dispersion and stabilization of small MNPs. Khaletskaya and co-workers deposited Au NPs onto the surface of MIL-125-NH₂ during the solvothermal synthesis of MIL-125-NH₂ [165]. Consequently, Au NPs/TiO₂ were fabricated through the pyrolysis of Au NPs/MIL-125-NH₂ under O₂ atmosphere at 450 °C (Fig. 17), and the photocatalytic activity for CO₂ reduction to CH₄ was significantly enhanced compared to pure TiO₂ and P25 under UV-light irradiation. Besides, the TiO₂ from MIL-125 pyrolysis could also play a role of photoanode in the dye-sensitized solar cells [166]. The obtained TiO₂ from MIL-125 pyrolyzed at 380 °C under air atmosphere possessed a large specific surface area of 147 m² g⁻¹ and a mean pore size of 10 nm. The overall energy conversion efficiency reached up to 7.2% when it was utilized as a photoanode material in dye-sensitized solar cells. Cake like anatase/rutile mixed phase TiO₂ (A/R TiO₂) with the size of about 500 nm was achieved from two pyrolytic section of MIL-125 under air atmosphere, first section was under 380 °C and the second was 500 °C [167], which almost reserved the intact microstructure of the MIL-125 crystal. The photocatalytic activity of A/R

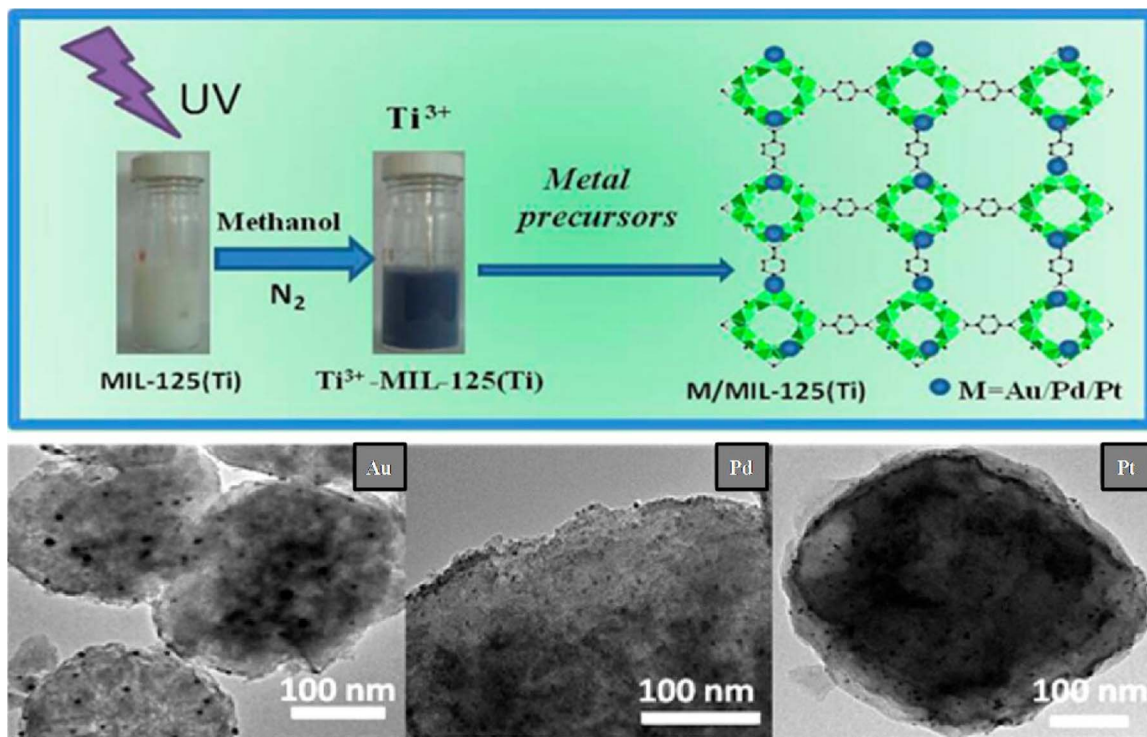


Fig. 16. Schematic presentation for the synthesis of M/MIL-125(Ti) (M = Au, Pd, Pt) composites and their TEM images[149].

TiO₂ for degradation of nitrobenzene was higher than that of the single anatase phase or rutile phase TiO₂. Following this study, they slightly changed the second section of pyrolysis in ammonia atmosphere and synthesized cake-like A/R N-TiO₂ [168]. The N-doping reduced the presence of stepwise energy levels in anatase and rutile TiO₂ [161], leading to the enhanced photocatalytic activity to RhB degradation under visible-light irradiation.

Pyrolyzation is a specific modification strategy for limited MOFs including MIL-125, ZIF-8 and ZIF-67. The control to crystal structure and integrity of frameworks are the key factors to the synthesis of high performance metal-oxide photocatalysts. But in some time, the photocatalytic activity after pyrolyzation would be decreased to some degree owing to the obviously reduced surface area and destructive structures.

4.1.5. Incorporation with other functional materials

Except the above-mentioned types of decoration of MIL-125 for photocatalysis, there are also other minority strategies to modify MIL-125, such as dye sensitization [169], decorated by RGO [170] and molecular photocatalysts encapsulation [171,172]. MIL-125-NH₂ has

been post-synthetically functionalized with methyl red [169]. The new material exhibited an increased absorption over a wide range of the visible spectrum, leading to the enhanced photocatalytic performance for the selective photo-oxidation of benzyl alcohol under visible-light irradiation. Up to now, examples of cooperative action between a MOF matrix and encapsulated molecular photocatalysts are very infrequent [171,172] due to the harsh terms of the choices of molecular catalysts and MOFs topology. The three conditions of the guest@MOFs composite should be satisfied: (1) photoresponsive struts for fast light-harvesting, (2) redox-active (multi) metallic nodes to allow charge-separation and accumulation of electrons, (3) an appropriate MOFs topology (i.e. large cavities connected by smaller windows) to encapsulate a molecular complex/nanocluster for productive turnover [171]. In 2015, through introducing a derivative of the well-known molecular Co-based electrocatalyst Co-dioxime-diimine (Co^{III}Br₂(L^H)) into the pores of MIL-125-NH₂ (denoted as Co@MIL-125-NH₂) following a 'Ship-in-a-bottle' strategy, Nasalevich and co-workers synthesized a highly active photocatalyst for the H₂ production from water under visible-light irradiation [171]. As shown in Fig. 18a, a direct

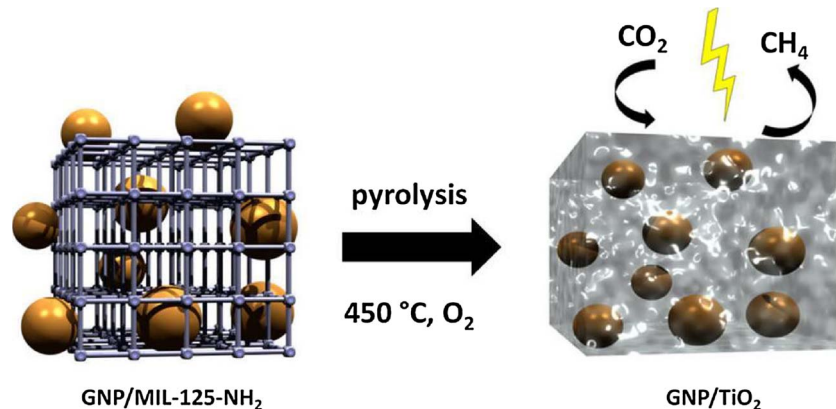


Fig. 17. Schematic diagram of the synthesis and photocatalytic reaction of GNP/TiO₂ [165].

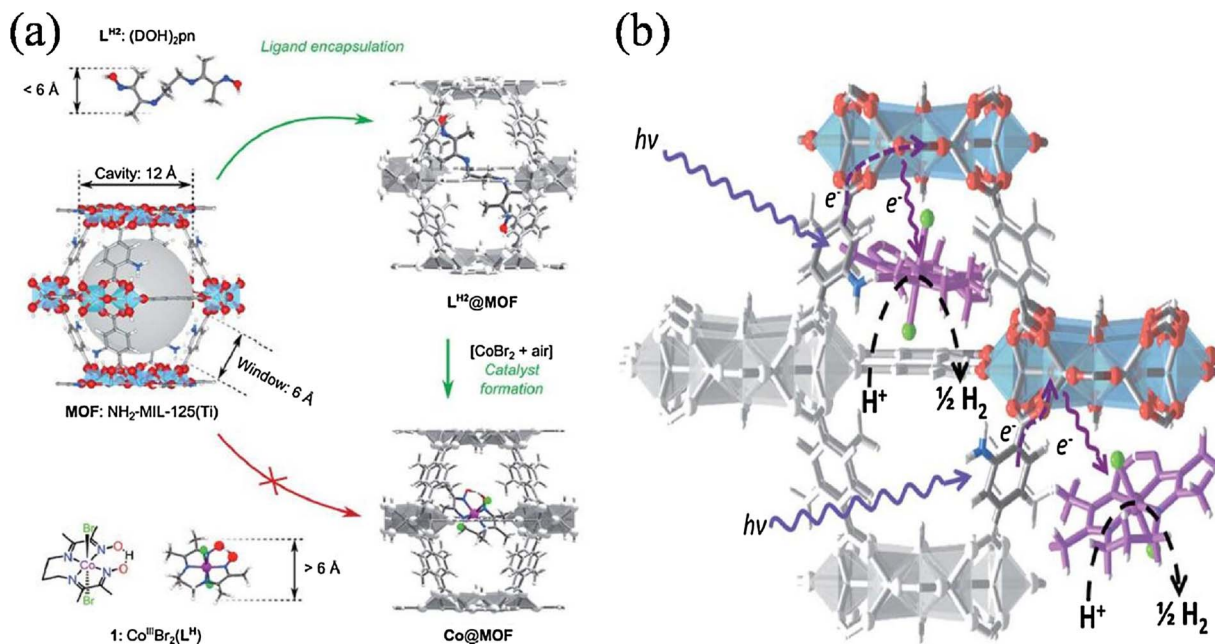


Fig. 18. 'Ship-in-a-bottle' synthetic strategy followed for assembling of Co@MOF (a), photocatalytic H₂ production using a multifunctional Co@MOF photocatalyst (b) [171].

encapsulation of Co^{III}Br₂(L^H) into MIL-125-NH₂ was unachievable due to the bigger size (> 6 Å), which was unable to enter into the interior of MIL-125-NH₂ framework from the window (6 Å). Therefore, the design of two-stage 'ship-in-the-bottle' strategy was needed. The flexible organic component (DOH)₂pn(L^H) (< 6 Å) was firstly encapsulated into the framework of MIL-125-NH₂, and then the Co^{III}Br₂(L^H) was assembled after addition of CoBr₂ under aerobic conditions within the large cavities of MIL-125-NH₂. The band gap energy of prepared Co@MIL-125-NH₂ composites is 2.59 eV. When the visible light irradiated, the internal electrocatalyst Co^{III}Br₂(L^H) could accept the photo-excited electrons from the LUMO of MIL-125-NH₂ and the photocatalytic H₂ production happened on its surface (Fig. 18b). Introduction of the molecular Co catalytic active site led to a 20-fold enhancement in H₂ production compared with the pristine MIL-125-NH₂. Similarly, [Co^{II}(TPA)Cl][Cl] (TPA = tris(2-pyridylmethyl)-amine) was also encapsulated into the cages of MIL-125-NH₂ by two-stage 'ship-in-the-bottle' strategy for visible-light-driven H₂ production in 2016 [172].

Overall, MIL-125 is one of the most popular MOFs in photocatalysis due to its stability in aqueous media and both photo- and redox-active multinuclear Ti-centers. In consideration of this, MIL-125 is more suitable than UiO-66 for utilizing as photocatalyst. However, research on various decoration methods is insufficient, especially on the strategy of combination with semiconductor. Many strategies to UiO-66 modification as photocatalysts would be worthy to attempt on MIL-125. Thus, MIL-125 holds a significant potential, which is very likely to surpass that of UiO-66 in the future. The modified strategies of MIL-125 and their corresponding applications are listed in Table 3.

4.2. MIL-101, MIL-100 and MIL-53

In 2005, the mesoporous chromium terephthalate MIL-101 (Cr₃F(H₂O)₂O[BDC]₃·nH₂O, BDC = terephthalic acid) was firstly synthesized by Ferey and co-workers and the Cr MOFs showed good resistance to air, water, popularly-used solvents and heat stability up to 300 °C [173]. MIL-101 has two kinds of zeotype quasi-spherical cages with free internal diameters of ca. 29 and 34 Å and microporous windows of ca. 12 and 16 Å. It has an extremely large surface area (2909.85 m² g⁻¹) [174] and numerous potential coordinatively unsaturated sites [175]. More importantly, MIL-101 is one of the typical MOFs with visible-light response [174,176–179], which is ascribed to the d-d spin-allowed

transition of the Cr³⁺ (d⁵) [180]. MIL-100, a Fe (III) containing MOF built up from Fe-O octahedra clusters and benzene-1,3,5-tricarboxylic acid, has been firstly prepared by Horcajada and co-workers in 2007 [181]. Due to the high thermal (~270 °C), photo, chemical and water stability, especially the response to visible light (band gap energy: 1.8 eV [182]) [65,181,183], MIL-100 has been selected as a representative MOF for visible-light-driven photocatalysis. MIL-53 possesses three isostructures: different metal center (Fe, Cr and Al) with the same organic linkers H₂BDC [184–186]. All of them are chemical, thermal stability and low toxicity. The onset of the main absorption edge of MIL-53(Fe), MIL-53(Cr) and MIL-53(Al) was 455, 395 and 320 nm, corresponding to the band gaps of 2.72, 3.20 and 3.87 eV, respectively [51]. Among them, MIL-53(Fe) were aroused extremely interest, since it is visible-light-response and iron is an earth-abundant element. MIL-53(Fe) is a three-dimensional porous solids composed of infinite FeO₄(OH)₂ clusters connected by H₂BDC ligand [187]. The visible-light responsive property implies that MIL-101, MIL-100 and MIL-53 can act as a visible-light active photosensitizer, which determines that most photocatalytic reactions based on them can be carried out under visible-light irradiation.

The studies of MILs utilizing as photocatalysts are mainly concentrated on: decoration of linker [188,189], combination with semiconductors [174,176,178,179,182,190–200], MNPs loading [177,196,201–208], decoration by RGO and GR [209–212], and incorporation with other functional materials [213,214].

4.2.1. Decoration of linker

The studies of linker decoration mainly focused on MIL-53. Although MIL-53(Fe) can absorb visible light, the photocatalytic activity could still be improved to a certain degree via the linker decorated by amino. Shi and co-workers confirmed that the amine-functionalized MIL-53(Fe)-NH₂ exhibited an enhanced visible-light absorption and photocatalytic activity for Cr(VI) photocatalytic reduction compared to MIL-53(Fe). An and co-workers synthesized two Al based MOFs (MIL-53(Al) and MIL-53(Al)-NH₂) and investigated their photoelectrical, photophysical and photocatalytic properties in oxygen evolution from water [189]. According to the results of theoretical calculation, steady state and time resolved fluorescence spectra, a new photocatalytic mechanism based on electron tunneling was proposed, which was different from the LMCT theory.

Table 3
Modified strategies of MIL-125 and their corresponding applications.

Strategies	details	MOF	Applications	Light source	Ref.
Decoration of linker	-NH ₂	MIL-125	CO ₂ , Cr(VI) reduction	Visible	[45,129]
	-NH ₂	MIL-125	Amines oxidation	Visible	[126]
	-NH ₂	MIL-125	Alcohols oxidation	Visible	[127]
	-NH ₂	MIL-125	N-hydroxy-carbamates	UV-vis	[130]
	-NH ₂	MIL-125	PCVG	UV	[131]
	-AM-Eu	MIL-125-NH ₂	Alcohols oxidation	UV-vis	[132]
	NHMe, NHEt, NHPr	MIL-125-NH ₂	CO ₂ reduction	Visible	[133]
	g-C ₃ N ₄	MIL-125	RhB degradation	Visible	[136]
	g-C ₃ N ₄	Ag/MIL-125	Nitrobenzene reduction and alcohols oxidation	Visible	[138]
	g-C ₃ N ₄	NiPd/MIL-125	H ₂ production	Visible	[139]
Combination with semiconductors	CFB	MIL-125-NH ₂	H ₂ production	Visible	[141]
	In ₂ S ₃	MIL-125	Tetracycline degradation	Visible	[144]
	BiOBr	MIL-125-NH ₂	RhB degradation	Visible	[145]
	PHIK	MIL-125-NH ₂	RhB degradation	Visible	[146]
	TiO ₂	MIL-125	Solar cell	Solar light	[142]
	TiO ₂	MIL-125-NH ₂	Photoelectrochemical sensor	Visible	[143]
	Pt, Au	MIL-125	H ₂ , formate production	Visible	[148]
	Au, Pd, Pt	MIL-125	H ₂ production, alcohols oxidation	UV-vis	[149]
	Ag	MIL-125	RhB degradation	Visible	[153]
	Ag	RGO/MIL-125	RhB degradation	Visible	[152]
MNPs loading	Ni	MIL-125-NH ₂	H ₂ production	UV	[155]
	Ag	MIL-125-AC	MB degradation	Visible	[151]
	Pt	MIL-125-NH ₂	Photocathode, H ₂ production	Visible	[147,150]
	Ni	MIL-125-NH ₂	Alcohols oxidation	Visible	[154]
	TiO ₂	MIL-125	Photoanode	UV-vis	[166]
	TiO _x /C	MIL-125	MB degradation	UV	[164]
	GNP/TiO ₂	GNP/MIL-125-NH ₂	CO ₂ reduction	UV	[165]
	A/R TiO ₂	MIL-125	Nitrobenzene degradation	UV	[167]
	A/R N-TiO ₂	MIL-125	RhB degradation	Visible	[168]

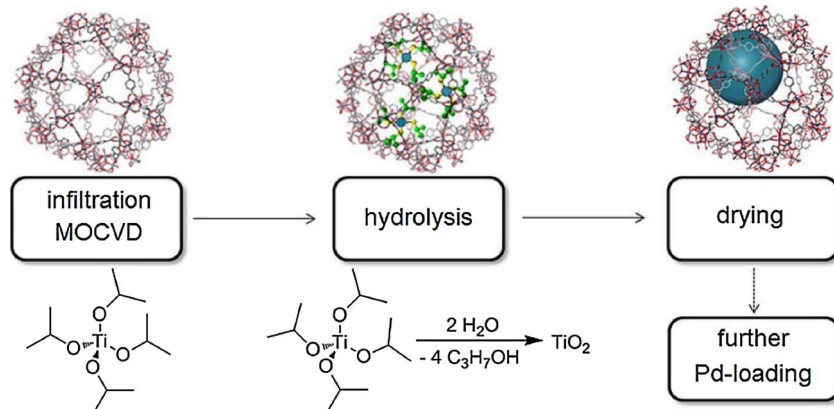


Fig. 19. Preparation of TiO₂@MIL-101 by MOCVD [192].

4.2.2. Combination with semiconductors

The earliest semiconductor combining with MIL-101 and MIL-100 is CdS. In 2013, He and co-workers demonstrated that embedding of CdS NPs (2–3 nm) on MIL-101 could significantly increase the photocatalytic efficiency of CdS for the visible-light-promoted hydrogen production when using Pt as co-catalyst [174]. The effective dispersion of CdS particles and the sensitization of CdS by MIL-101 were responsible for the enhanced photocatalytic activity. Besides, they demonstrated that the photo-induced electrons were transferred from the CB of MIL-101 to that of CdS because the lower CB potential of MIL-101. Jiang and co-workers introduced polyoxo-titanium clusters into the CdS/MIL-101 system that resulted in a highly efficient visible-light-range H₂-evolution photocatalysts [191]. The introduced polyoxo-titanium acted as a mediator to transfer the photo-induced electrons between CdS and MIL-101. It remains controversial that the transfer direction of electrons was from CB of CdS to that of MIL-101 in this report. Similarly, MIL-100 combined with CdS was synthesized via a solvothermal method by Ke and co-workers in 2015 [182]. The prepared CdS-MIL-

100 nanocomposites exhibited enhanced visible-light photocatalytic activity for the selective oxidation of benzyl alcohol to benzaldehyde. Meantime, He and co-workers made CdS NPs be dispersed and embedded on MIL-100 for photocatalytic degradation of nitrite ions through a disproportionation in a neutral aqueous solution without any sacrificial reagents [195]. The photo-induced electrons reduced NO₂[–] to yield the NH₄⁺ and the holes oxidized NO₂[–] to produce NO₃[–] at the same time. When 20 wt% of CdS was embedded on MIL-100, the degradation yield was five folds to bare CdS. The enhancement in photocatalytic activities was ascribed to photosensitization and supporting of MIL-100 scaffold. Very recently, a Co-Ni sulfide Co₂Ni₂S₄@MIL-101 exhibited an outstanding photocatalytic activity for H₂ production (882.7 μmol in 120 min) after sensitized by Eosin Y under visible-light irradiation at pH 9 [194]. The high photocatalytic efficiency was ascribed to the low ΔG_H over Co₂Ni₂S₄, stable reaction intermediate during hydrogen formation and better photoelectrochemical properties.

Due to the property of visible-light response, MIL-101 and MIL-100 even could incorporate with semiconductor with no visible-light

absorption, e.g. TiO_2 [178,179,190,192,199]. In 2015, the controlled incorporation of nanoscale palladium and titanium dioxide inside MIL-101 was accomplished by metal-organic chemical vapor deposition (MOCVD) (Fig. 19) [192]. The Ti-precursor $[\text{Ti}(\text{O}-\text{iP})_4]$ was infiltrated into MIL-101 by MOCVD and thermally decomposed to titania under water atmosphere. Subsequently, the same gas-phase loading of $[(\text{C}_5\text{H}_5)\text{Pd}(\text{C}_3\text{H}_5)]$ and reduction by hydrogen gave rise to $\text{Pd}/\text{TiO}_2@\text{MIL-101}$ composites. The prepared $\text{Pd}/\text{TiO}_2@\text{MIL-101}$ showed efficient photocatalytic activity in hydrogenation and dehydrogenation. Subsequently, they prepared the MIL-101-core-Au/anatase-shell photocatalyst for visible-light-driven degradation of dyes and the antibiotic ciprofloxacin from wastewater [179]. In order to further improve the absorption of visible light by MIL-101-NH₂, Li and co-workers modified it with salicylaldehyde and made TiO_2 be encapsulated [178]. The conjugated linker was elongated and the resulting framework showed enhanced absorption of visible light. The MB degradation was dramatically enhanced from 30% of $\text{TiO}_2@\text{MIL-101-NH}_2$ to 86% of $\text{TiO}_2@\text{Salicylaldehyde-MIL-101-NH}_2$. $\text{TiO}_2@\text{MIL-101}$ core-shell composites were also fabricated for the adsorption and photocatalytic degradation of MO by Chang and co-workers [190]. Designing and building hierarchically porous structures through assembling 2D TiO_2 NS with MOFs was verified as an ideal solution to create a large number of functional interfaces [215]. Based on this, a hierarchical sandwich-like TiO_2 NS@MIL-100 heterostructure was developed through a self-assembled method by incorporating MIL-100 into TiO_2 NS [199]. The nanocomposites exhibited good adsorption capacity and enhanced visible-light photocatalytic degradation of MB due to the porous MIL-100 loading and the sandwich-like heterostructure that provides a platform for high-speed interfacial photogenerated charges transfer. $\text{H}_3\text{PMo}_{12}\text{O}_{40}$, a typical Keggin-type polyoxometalates, was encapsulated in the pores of MIL-100 for the selective oxidation of alcohols and the reduction of heavy metal ions Cr(VI) under visible-light irradiation by Liang and co-workers [216]. They found that $\text{H}_3\text{PMo}_{12}\text{O}_{40}$ acted as the major photocatalyst in the selective oxidation system while MIL-100 played the key role in the Cr(VI) reduction process.

$\text{N-K}_2\text{Ti}_4\text{O}_9$ [176] was also been investigated to incorporate with MIL-101 for MB degradation under visible-light irradiation. MIL-100 grown on g-C₃N₄ nanosheets for the photocatalytic degradation of RhB was reported by Hong and co-workers [197]. Bismuth-based semiconductors such as BiWO_4 and Bi_2MoO_6 were successfully incorporated into MIL-100 for the visible-light photocatalytic degradation salicylic acid [198] and RhB [200], respectively. Zheng and co-workers proved that p-n junction formed by n-type semiconductor BiWO_4 and p-type MIL-100 could facilitate the photogenerated charge separation [198].

4.2.3. MNPs loading

MNPs loading on MILs is the other major direction for utilizing MILs as photocatalysts. Pt NPs were firstly incorporated into MIL-101-NH₂ for the visible-light-driven H₂ production with RhB sensitization in 2014 [201]. The porous MIL-101-NH₂ not only served as electric conductors to promote the electron transfer, but also acted as photo-electron generators through LMCT mechanism. Ni/NiO_x particles instead of noble metals were *in situ* photodeposited on MIL-101 for boosting H₂ generation with Erythrosin B dye sensitization under visible-light irradiation [202]. $\text{Pd}/\text{MIL-101}/\text{rGO}$ was fabricated for degradation of two triphenylmethane dyes, brilliant green and acid fuchsin [203].

Similar to the preparation of $\text{Ag}/\text{AgCl}@\text{ZIF-8}$ [217–219], Gao and co-workers synthesized $\text{Ag}/\text{AgCl}@\text{MIL-101}$ hetero-junction photocatalyst via a vapor diffusion-photoreduction process [177]. The photocatalytic activity was evaluated for the degradation of RhB under visible-light irradiation. However, most of the Ag/AgCl stuck on the external surface of the MIL-101 with large sizes of 200–500 nm due to the high speed reaction between Ag⁺ and Cl⁻ ions. To solve this problem, Yan and co-workers introduced a Ag monosubstituted polyoxometalate (POM), $\text{K}_6[\alpha\text{-AgPW}_{11}\text{O}_{39}]$, into MIL-101(Al)-NH₂ through an incipient wetness impregnation method and subsequent photo-

reduction under UV irradiation to obtain $\text{Ag}/\text{POM-AgCl}@\text{MIL-101(Al)-NH}_2$ composite [205]. Mono-vacant POMs could coordinate with Ag⁺ ions, which may control the growth of Ag/AgCl nanocrystals. The as-obtained $\text{Ag}/\text{POM-AgCl}$ composite NPs possessed an average particle size of 3.2 nm and the $\text{Ag}/\text{POM-AgCl}@\text{MIL-101(Al)-NH}_2$ showed higher photocatalytic activity for RhB degradation than that of $\text{Ag}/\text{AgCl}@\text{MIL-101(Al)-NH}_2$. PNPMOF was self-assembled by a polyoxometalate (POM), Pt NPs and MIL-53(Al)-NH₂, which displayed enhanced activity for visible-light-driven catalytic H₂ production [220].

The alloyed catalysts could regulate electronic structures and enhance catalytic activity [221]. A highly efficient photocatalyst NiMo@MIL-101 for the H₂ production was fabricated by the double solvents method according to the advanced DFT and frontier molecular orbital theory calculation analysis [206]. Compared with Ni@MIL-101 and Mo@MIL-101, the resulting NiMo@MIL-101 showed an excellent photocatalytic performance (740.2 $\mu\text{mol h}^{-1}$ for H₂ production), stability and highly apparent quantum efficiency (75.7%) under 520 nm-light illumination at pH 7. They also demonstrated that the lower ΔG_{H} of Ni-Mo (MoNi₄) alloy nanoclusters led to the higher H₂ production activity. To sensitize Pd active sites and boost their intrinsic activity of Pd under visible-light irradiation, constructing PdAu bimetal hetero-structures was a feasible way because of the visible-light absorption and higher electronegativity of Au. Wen and co-workers fabricated Au/Pd-MIL-101 photocatalysts for hydrolysis of ammonia borane and Suzuki-Miyaura coupling reaction under visible-light irradiation [204].

Liang and co-workers fabricated M@MIL-100 (M = Pd, Pt, Au) via a alcohol reduction approach for the visible-light photocatalytic degradation of three typical pharmaceutical and personal care products (PPCPs), theophylline, ibuprofen and bisphenol A [196]. The photocatalytic activities closely depended on the different types and contents of metal. The 1%Pd@MIL-100 exhibited the relatively high photocatalytic activity. In addition, the addition of H₂O₂ and pH value also influenced the photocatalytic reaction. Active species trapping experiments with different radical scavengers revealed that the photo-induced electrons and ·OH played major roles towards the degradation of PPCPs (Fig. 20). A photochemical route to synthesized M@MIL-100 (M = Pd, Pt, or Au) was developed for the photocatalytic degradation of MO and the reduction of Cr(VI) in water under visible-light irradiation [207]. In this photocatalytic system, Pt@MIL-100 with an average Pt particle size of 2 nm showed the highest photoactivity. Following this research line, Wang and co-workers developed a double-solvent impregnation way combined with a photoreduction process to prepare Pd@MIL-100 with 1.7 nm average size of Pd NPs confined inside the cavity of MIL-100 [208]. The resultant Pd@MIL-100 exhibited much higher photocatalytic activity in light-induced N-alkylation of amines with alcohols compared to that of Pd NPs with size of 6–12 nm loading on the external surface of MIL-100. The efficient coupling of photocatalytic dehydrogenation and Pd-based hydrogenation were responsible for the enhanced photocatalytic activity.

4.2.4. Decoration by GR or RGO

The reports of MIL-53 combining with graphene are intensive, including graphene (GR) and reduced graphene oxide (RGO). In 2015, Zhang and co-workers firstly fabricated GR hybridized MIL-53(Fe) microrods through a one-pot solvothermal method [210]. GR was derived from the reduction of GO during the solvothermal process. The GR/MIL-53 systems showed significantly higher photocatalytic activity for RhB degradation than that of bare MIL-53 under visible-light irradiation in the presence of H₂O₂ (Fig. 21). To seek a more efficient preparation method, MIL-53(Fe)-RGO was constructed by electrostatic self-assembly between negatively charged GO and positively charged MIL-53(Fe), followed by a solvothermal reduction of GO to RGO [209]. Compared with direct synthesis of MIL-53(Fe)-RGO via one-pot solvothermal approach, electrostatic self-assembly synthesized MIL-53(Fe)-RGO exhibited improved photocatalytic activity. In addition, MIL-53(Fe)-RGO nanocomposites were proven to be a bifunctional

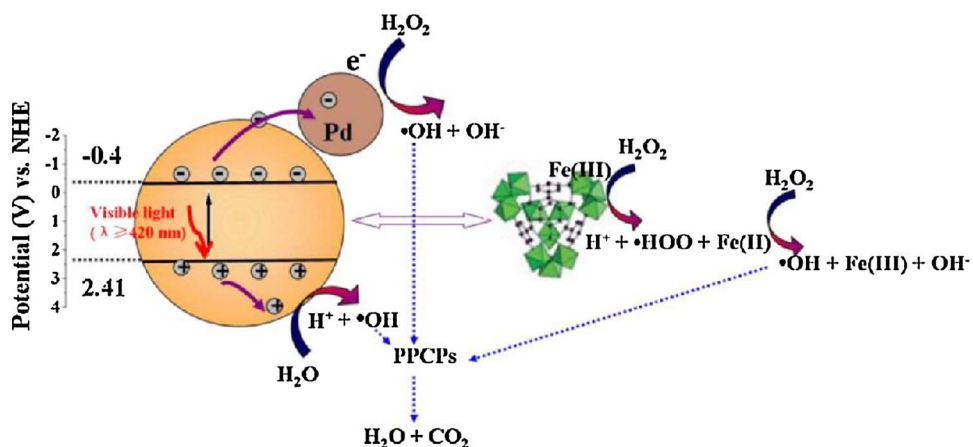


Fig. 20. Mechanism for the photocatalytic degradation of PPCPs over Pd@MIL-100(Fe) under visible-light irradiation [196].

photocatalyst with good activity in the mixed systems (Cr(VI)/dyes) under visible-light irradiation, which was similar to their previous reports [62,95]. A series of MIL-53(Fe)-GR were also synthesized for the photocatalytic selectively oxidation of alcohols to the corresponding aldehydes or ketones and the selectivity could reach 99% [211]. Recently, MIL-53(Al)-NH₂ nanocrystals were anchored on the surface of RGO hollow spheres for photocatalytic degradation of MB [212].

4.2.5. Incorporation with other functional materials

Recycling test is a very important index for catalysts in the practical applications. Compared to the conventional photocatalysts, the magnetic photocatalyst is green, cheap and more suitable for large scale industrial applications. Fe₃O₄ NPs possess good magnetic properties and low toxicity to the environment [222], offering facile recyclability and accessibility as catalysts. However, Fe₃O₄ is highly susceptible to photodissolution [214]. Thus, the core-shell structures with Fe₃O₄ as the core were feasible for photocatalysis [213,214]. The magnetic Fe₃O₄@MIL-100 core-shell microsphere was firstly fabricated by Zhang and co-workers in 2013 [213]. The photocatalytic activity for MB was much higher than that of TiO₂ and g-C₃N₄ with H₂O₂ addition not only under UV-vis light but also under visible-light irradiation. Zhao and co-workers investigated the effect of H₂O₂ addition and the thickness of MIL-100 shell to the photocatalytic degradation of MB in detail [214]. As shown in Fig. 22, H₂O₂ acted a photo-induced electrons accepter and the holes could transfer to Fe₃O₄ core that the efficiency depended on the thickness of MIL-100 shell. The optimal shell thickness was about 50 nm, corresponding to the highest photocatalytic activity.

Many other approaches to improve the photocatalytic activity of MILs were carried out as well. Polyoxometalate [Co

(H₂O)₂(PW₉O₃₄)₂]¹⁰⁻ incorporating in MIL-101 was studied for the water oxidation [193], showing that the effect of the polyoxometalate was for collecting and transferring electrons. After composited with anionic resin (Amberlite IRA 200) and cationic resin (Amberlite IRA 900), two types of MIL-53(Fe) equipped with negative and positive charge (AMIL-53 and DMIL-53) were synthesized respectively [223]. AMIL-53 and DMIL-53 showed reversed photocatalytic degradation to cationic and anionic dyes under visible-light irradiation. However, very few attention has been concentrated on the development of NIR–responsive MOF photocatalysts. Recently, NaYF₄:Yb,Tm/MIL-53(Fe) photocatalysts with a uniform core-shell structure have been synthesized through surface modification of the upconversion NPs and sequential coating of PVP polymer [224]. The prepared photocatalysts exhibited an enhanced activity for the degradation of RhB, MB and phenol under solar spectrum due to their response to the NIR light. A magnetic MIL-53(Fe) (MAG-MIL) has been prepared by an in-situ ethylenediamine-assisted solvothermal method [225]. The well dispersed γ-Fe₂O₃ NPs embedded in the MAG-MIL framework led to a red shift of the light absorption edge and showed good photocatalytic activity for the degradation of MB.

In summary, MILs hold a great potential application for photocatalysis under solar light due to their wide absorption in visible-light region. The modified strategies abound as to MILs, but the effect or purpose of a single strategy to them is limited, for instance, the modified methods to MIL-101 mainly focus on combination with semiconductor and MNPs loading, whereas other modification strategies referring to that of other MOFs (e.g. UiO-66, MIL-125 and ZIF-8) have not been carried out. Therefore, the photocatalytic reactions over various MILs remain at the infant stage and numerous modification

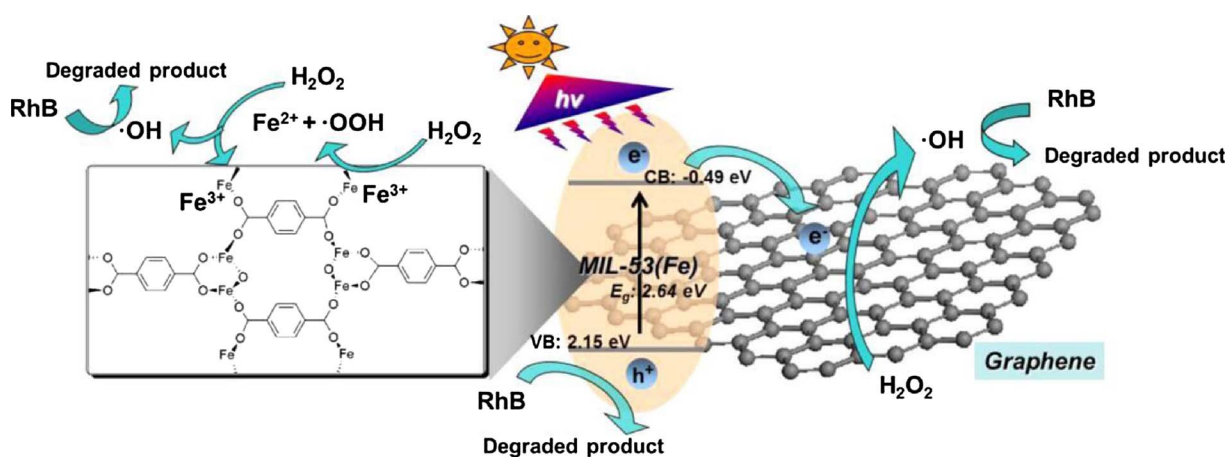


Fig. 21. Photocatalytic process of graphene/MIL-53(Fe) composite in the presence of H₂O₂ [210].

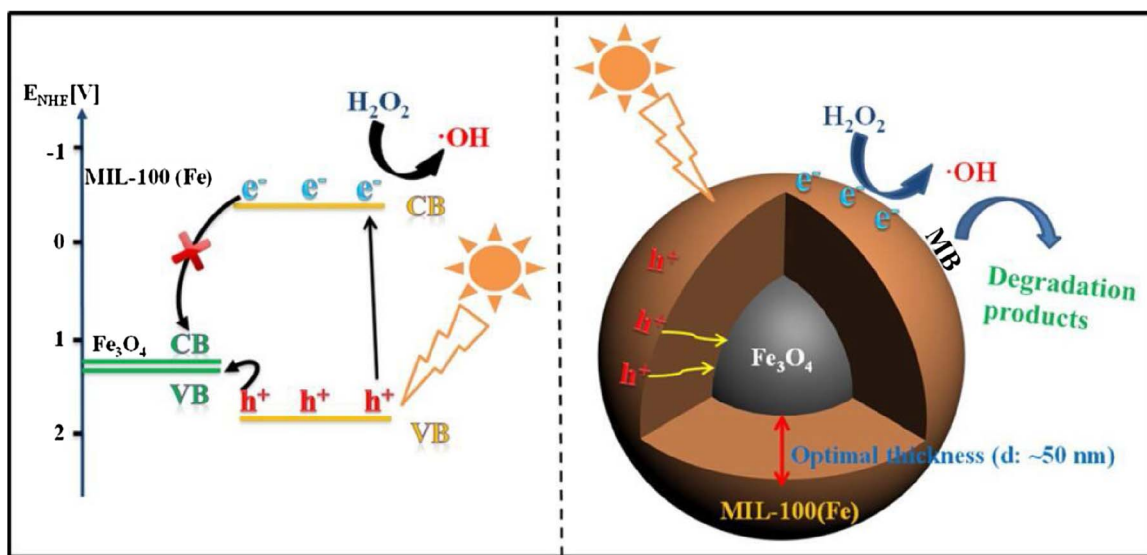


Fig. 22. The mechanism of photocatalytic degradation of MB over $\text{Fe}_3\text{O}_4@\text{MIL-100}$ [214].

Table 4

Modified strategies of MIL-101, MIL-100 and MIL-53 and their corresponding applications.

Strategies	details	MOF	Applications	Light source	Ref.
Decoration of linker	-NH ₂	MIL-53(Fe)	Cr(VI) reduction	Visible	[188]
	-NH ₂	MIL-53(Al)	O ₂ production	UV-vis	[189]
Combination with semiconductors	CdS	MIL-101	H ₂ production	Visible	[174]
	N-K ₂ Ti ₄ O ₉	MIL-101	RhB degradation	UV-vis	[176]
	CdS	PTC/MIL-101	H ₂ production	Visible	[191]
	TiO ₂	Salicylaldehyde/M IL-101-NH ₂	MB degradation	Visible	[178]
	TiO ₂	MIL-101	MO degradation	UV	[190]
	TiO ₂	Au/MIL-101	H ₂ production, antibiotics degradation	Visible	[179]
	TiO ₂	Pd/MIL-101	Hydrogenation and dehydrogenation	UV	[192]
	CdS	MIL-100	Nitride degradation	UV-vis	[195]
	CdS	MIL-100	Alcohols oxidation	Visible	[182]
	g-C ₃ N ₄	MIL-100	RhB degradation	Visible	[197]
MNPs loading	BiWO ₄	MIL-100	Salicylic acid degradation	Visible	[198]
	Bi ₂ MoO ₆	MIL-100	RhB degradation	Visible	[200]
	TiO ₂	MIL-100	MB degradation	Visible	[199]
	g-C ₃ N ₄	MIL-53(Al)	RhB degradation	UV-vis	[46]
	Pt	MIL-101-NH ₂	H ₂ production	Visible	[201]
	Ni	NiO _x /MIL-101	H ₂ production	Visible	[202]
	Pd	RGO/MIL-101	Triphenylmethane dyes degradation	Visible	[203]
	Ag	AgCl/ MIL-101	RhB degradation	Visible	[177]
	AuPd	MIL-101-NH ₂	Ammonia borane hydrolysis, Suzuki-Miyaura coupling reaction	Visible	[204]
	NiMo	MIL-101	H ₂ production	Visible	[206]
Decoration by RGO and GR	Au, Pd, Pt	MIL-100	MO degradation, Cr(VI) reduction	Visible	[207]
	Pd	MIL-100	PPCP degradation	Visible	[196]
	Pd	MIL-100	Amines N-alkylation	Visible	[208]
	RGO	MIL-53(Fe)	Cr(VI) reduction, dyes degradation	Visible	[209]
	RGO	MIL-53(Al)-NH ₂	MB degradation	UV-vis	[212]
	GR	MIL-53(Fe)	RhB degradation	Visible	[210]
	GR	MIL-53(Fe)	Alcohols oxidation	Visible	[211]

methods deserve to be attempted. The modified strategies of MIL-101, MIL-100 and MIL-53 and their corresponding applications are summarized in [Table 4](#).

5. ZIFs

As one of the most typical MOF materials, zeolitic imidazolate frameworks (ZIFs), constructed by the tetrahedrally coordinated divalent cations (Zn^{2+} or Co^{2+}) and imidazolate linkers, showed their capabilities in various fields [27,226–232]. Compared with the other MOFs, ZIFs not only have good thermal/chemical stability and water tolerance, but also possess tunable zeotype topologies and easy synthetic process to achieve uniform structures. Among them, ZIF-8(Zn)

and ZIF-67(Co) are two typical ZIFs utilized for photocatalyst, especially ZIF-8. However, the large band gap energy (5.1 eV) and the fixed organic linkers limit its photocatalytic activity of ZIF-8 under visible light. On the contrary, ZIF-67 has a low band gap ($E_g = 1.98$ eV) and multiple absorption bands in the UV-vis-near IR region [72,233]. The studies about ZIF-8 for photocatalysis are much more than that of ZIF-67, probably because the easy-controlled synthesis and large researched space of ZIF-8 relatively.

5.1. Partial substitution of metal center

The linker of ZIFs is imidazolate, which is comparatively difficult to modify. Thus, the modifications at the molecule level of ZIFs were

concentrated on the metal center partial substitution. Early in 2012, a Cu doping strategy was applied to tune the gas sorption and photocatalytic properties of ZIF-67 [233]. Results demonstrated that Cu substituted ZIF-67 showed high H₂ and CO₂ uptake capacities and highly efficient degradation of MO under visible-light irradiation. Later, the active Ni metal was introduced into the metal center of ZIF-8 via a one-pot mechanochemical method under liquid assisted grinding conditions [234]. This Ni-substituted ZIF-8 adopted topology of ZIF-8 with Ni partially substituting the ZnN₄ in the backbone. The samples with photoactive Ni centers and open channels exhibited outstanding photocatalytic activity for the degradation of MB under visible light.

5.2. Combination with semiconductors

For ZIF-8, combination with semiconductors always realized over a designed route and ZIF-8 was growing on the surface of semiconductor with a diversity of morphologies in most cases. Liu and co-workers firstly found that ZIF-8 could effectively adsorb CO₂ dissolved in water and constructed a Zn₂GeO₄/ZIF-8 nanocomposite for the photocatalytic conversion of CO₂ into liquid CH₃OH fuel [232]. The composites were prepared by growing ZIF-8 NPs on Zn₂GeO₄ nanorods. The prepared Zn₂GeO₄/ZIF-8 hybrid nanorods with 25 wt% ZIF-8 contents exhibited 3.8 times CO₂ adsorption capacity as high as that of bare Zn₂GeO₄ nanorods and 62% enhancement in the photocatalytic conversion rate. Core-shell ZnO@ZIF-8 nanospheres were synthesized by a self-template method [235], where ZnO not only acted as the template but also supplied Zn(II) for the composition of ZIF-8. The photocatalytic degradation of MB was dominated by the outer ZIF-8 shell for the molecule size of MB is larger than the pore aperture of ZIF-8. Similarly, utilizing the molecule size selectivity of ZIF-8 shell, Wang and co-workers adopted the same method to construct the ZnO@ZIF-8 heterostructures for the selective reduction of Cr(VI) between Cr(VI) and MB [236] under UV-light irradiation (Fig. 23). The photoreaction active sites were located on ZnO sphere where only CrO₄²⁻ could go through the aperture of the ZIF-8 frameworks. During the synthesis process of ZnO@ZIF-8 heterostructures, they found that the concentration of organic ligand 2-methylimidazole was crucial for the preparation of core-shell heterostructures by remarkably influencing the balance between the rate of ZnO dissolution and the rate of Zn²⁺ coordination. Subsequent work has also been carried out based on ZnO/ZIF-8 composites for photocatalytic degradation of organic dyes [237].

In order to study the effect of the interfacial reaction between semiconductors and MOFs, ZIF-8 was assembled homogeneously on the surface of electrostatic spinning TiO₂ nanofibers and formed a N–Ti–O bond under sonochemical treatment [215] without surfactants or

additives (Fig. 24). The newly formed chemically bond between TiO₂ and ZIF-8 highly promoted the thermal stability, crystallinity and photocatalytic activity in RhB photocatalytic degradation compared to commercial P25. Three factors account for the enhanced photoactivity: (1) More light would be harnessed by the outer ZIF-8 shell with light penetration and scattering properties, (2) ZIF-8 played a role of cocatalyst together with TiO₂ and (3) chemical-bonds of N–Ti–O suppressed the recombination of photo-excited electron-hole pairs. In 2017, ZIF-8 NPs were deposited on the surfaces of mesoporous TiO₂ nanobeads for the photocatalytic reduction of Cr(VI) [238]. The enhanced photocatalytic activity was ascribed to the strong Cr(VI) adsorption property of ZIF-8 as well as more efficient charge transfer compared to pristine TiO₂ beads. Similarly, ZIF-8 nanoclusters were grown on the g-C₃N₄ nanotubes as well for the CO₂ photocatalytic reduction [239]. The yield of methanol over g-C₃N₄/ZIF-8 composite reached to 0.75 μmol h⁻¹ g⁻¹ that was about 3 times than that of pure g-C₃N₄. The excellent CO₂ adsorption by grafting additional ZIF-8 nanoclusters was responsible for the enhanced photocatalytic activity. However, the conductivity of most MOFs is not good enough, which limited the charge transfer to a certain degree. Thus, the loading amount of MOFs is a crucial parameter for photocatalysis. The nanosheets of g-C₃N₄ were also anchored onto ZIF-8 microstructures and a highly stable micro-meso porous architecture was formed for the adsorption and photocatalytic degradation of tetracycline [240]. To integrate dual photothermal- and catalytic-functionality, a core-shell hierarchical Cu₇S₄ nano-heater@ZIF-8 heterostructures were prepared for the cyclocondensation reaction under laser irradiation (1450 nm) [241]. Near-infrared LSPR of Cu₇S₄ NPs core was responsible for the improved photocatalytic activity.

5.3. MNPs loading

The design of MNPs loading on ZIF-8 as photocatalysts is based on three points: (1) ZIF-8 provides a large specific surface area and would efficiently adsorb reactants [217–219,242,243]; (2) ZIF-8 as shell could play a “molecular sieve” role for reactants with specific sizes and stabilize the MNPs core for excellent recyclability [242,243], and (3) The photocatalytic activity mainly depends on the LSPR effect of MNPs due to the none photocatalytic activity of ZIF-8, especially under visible-light irradiation [217–219,242,243]. The LSPR effect enhances the activity of photocatalysts by extending light absorption to longer wavelengths and transferring the plasmonic electrons from the SPR metal to the CB of semiconductor [244].

Ag/AgCl NPs can harvest solar energy in a very broad visible spectra region due to the LSPR effect of Ag NPs. However, the photocatalytic

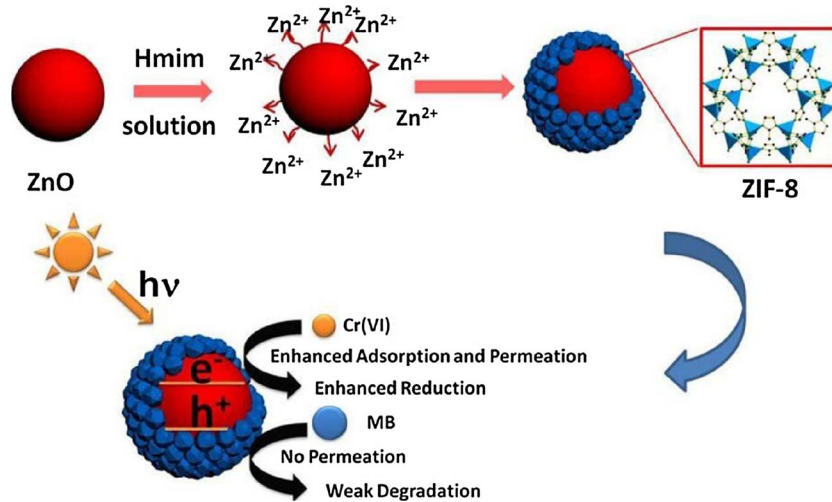


Fig. 23. The construction of ZnO@ZIF-8 and its selective photocatalytic reduction of Cr (VI) [236].



Fig. 24. The constructed process of TiO₂/ZIF-8 nanofibers (NFs) [215].

activity of Ag/AgCl under visible-light irradiation is limited by its poor adsorption capacity and relatively weak reducing capacity [219]. Thus, loading them on ZIF-8 is a feasible way to address these problems [217–219]. Ag/AgCl@ZIF-8 was firstly fabricated by depositing the Ag/AgCl on the surface of ZIF-8 [217]. The photo-induced electrons could transfer from Ag/AgCl to ZIF-8 though the CB position of ZIF-8 (−0.86 eV vs NHE) is very low. The prepared Ag/AgCl@ZIF-8 showed enhanced photocatalytic activity for the RhB degradation under visible-light irradiation. Liu and co-workers also synthesized Ag/AgCl/ZIF-8 for the photocatalytic degradation of RhB and the mechanism has been investigated thoroughly [219]. Meanwhile, they constructed Ag@AgCl/Ag nanofilm/ZIF-8 composites by loading Ag@AgCl and Ag nanofilm on the surface of ZIF-8 simultaneously via a deposition–photoreduction method [219]. The extended contact interface between Ag nanofilm and ZIF-8 promoted the quick electrons transfer and electron–hole pairs separation, leading to a remarkable improvement of photocatalytic activity for the degradation of MB. The encapsulation MNPs into the cavity of ZIF-8 is a typical design and has the merits of molecular sieving effect and high stability of metal nanoparticals. Chen and co-workers utilized PVP-Au NPs as nucleation seeds for ZIF-8 to selectively synthesize Au@ZIF-8 single- or multi-core-shell structures by epitaxial growth or coalescence of nuclei (Fig. 25a) [243]. The photocatalytic performance was evaluated by the oxidation of benzyl alcohol and the low conversion over Au@ZIF-8 compared to Au-SiO₂ was ascribed to the size-selectivity of ZIF-8. Recently, a core-shell Pd nanocubes (NCs) @ZIF-8 was utilized for the selective photocatalysis of the small olefins hydrogenation (Fig. 25b) [242]. The catalytic activity under 100 mW cm^{−2} visible-light irradiation at ambient temperature was the same as that of thermally driven (no light) catalytic hydrogenation at 50 °C.

5.4. Sensitization

Although ZIF-67 possesses a small band gap ($E_g = 1.98$ eV), the efficiency for visible-light-driven photocatalysis of ZIF-67 is low when using single-component ZIF-67 due to the limited absorption in the solar spectrum. Its relatively small extinction coefficients of Co²⁺ d-d transitions ($\sim 100\text{--}1000 \text{ mol L}^{-1} \text{ cm}^{-1}$) cause for this defect [245]. Expanding the absorption spectrum of ZIF-67 through sensitization by a chromophore is a desirable strategy that is similar to dye sensitization. Qin and co-workers synthesized ZIF-67 as a co-catalyst for photochemical CO₂ reduction under visible-light irradiation by cooperation of dye photosensitizer [Ru(bpy)₃]Cl₂·6H₂O (bpy = 2'2'-bipyridine), using triethanolamine (TEOA) as electron donor [246]. The CO generation rate reached to 74.8 $\mu\text{mol h}^{-1}$, which was much higher than that of other types of MOFs (ZIF-8, UiO-66-NH₂ and MIL-101-NH₂) (Table 5). A porous hybrid system by sensitizing the RuN₃

photosensitizer on the surface of ZIF-67 for H₂ production from water has been reported by Yang and co-workers [245]. According to the transient absorption spectroscopy, the energy transferred efficiency from the excited RuN₃ to ZIF-67 reached to ~86.9%, leading to the enhanced photocatalytic activity.

5.5. Pyrolyzation

ZnO is a technologically important II–VI semiconductor with a wide direct band gap of 3.37 eV and a large excitation binding energy of approximately 60 mV [247]. Besides, ZnO has a higher electron mobility of 115–155 $\text{cm}^2 \text{ V}^{-1} \text{ s}^{-1}$ compared to that of TiO₂ (only $10^5 \text{ cm}^2 \text{ V}^{-1} \text{ s}^{-1}$ for the most used TiO₂) [248], suggesting ZnO particles or clusters may serve as the good electron trappers and transmission medium. Similar with TiO₂ derived from MIL-125, the pyrolysis of ZIF-8 to ZnO with porous structure for photocatalysis also plays an important role and the studies were more than that of MIL-125. The pyrolysis of ZIF-8 had two strategies: one-step pyrolysis and two-step pyrolysis. The prepared ZnO were almost C/N doped, due to C and N doping could generally render electrons lighter and holes heavier, resulting in more visible-light harvesting and decreased recombination rate of photo-induced electron–hole pairs [249].

One-step pyrolysis of ZIF-8 is rapid and simple. The C-ZIF/g-C₃N₄ composite was constructed via thermal condensation of ZIF-8 and melamine at 650 °C under N₂ flow [250]. The C-ZIF/g-C₃N₄ composite with 1 wt% C-ZIF onto g-C₃N₄ showed highest photocatalytic activity for the H₂ production under visible-light irradiation, which was 36.2 times higher than that of pure g-C₃N₄ and 2.8 times higher than that of Pt/g-C₃N₄. The C-ZIF derived from the pyrolysis of ZIF-8 acted as a bifunctional electron acceptor and H₂ production reaction cocatalyst in the photocatalytic H₂ production. Mesoporous ZnO with the bimodal carbon modification (carbon doping and surface carbon coating) was prepared simultaneous during the pyrolysis of ZIF-8 in air [251]. The sample calcined at 500 °C showed the highest photocatalytic CO₂ reduction activity (0.83 $\mu\text{mol h}^{-1} \text{ g}^{-1}$), which was about six folds higher than that of ZnO nanorods synthesized by a hydrothermal method. Porous N-doped ZnO through direct calcination of ZIF-8 and urea mixture was also prepared at 550 °C [231]. The photocatalytic activity for RhB degradation was 2.58 times higher than that of ZIF-8-derived ZnO under visible-light irradiation. To accurately investigate the contents and types of nitrogen in the calcined ZIF-8, Zhao and co-workers prepared N-doped graphene analogs by calcining ZIF-8 under Ar atmosphere at different temperatures [252]. After the pyrolysis of ZIF-8, the N-doped graphene analogs not only retained the polyhedron structure but also possessed nitrogen contents of 9–15 wt% depending on the calcination temperature. In addition, the total and relative contents of graphitic nitrogen, pyridinic nitrogen and pyrrolic nitrogen

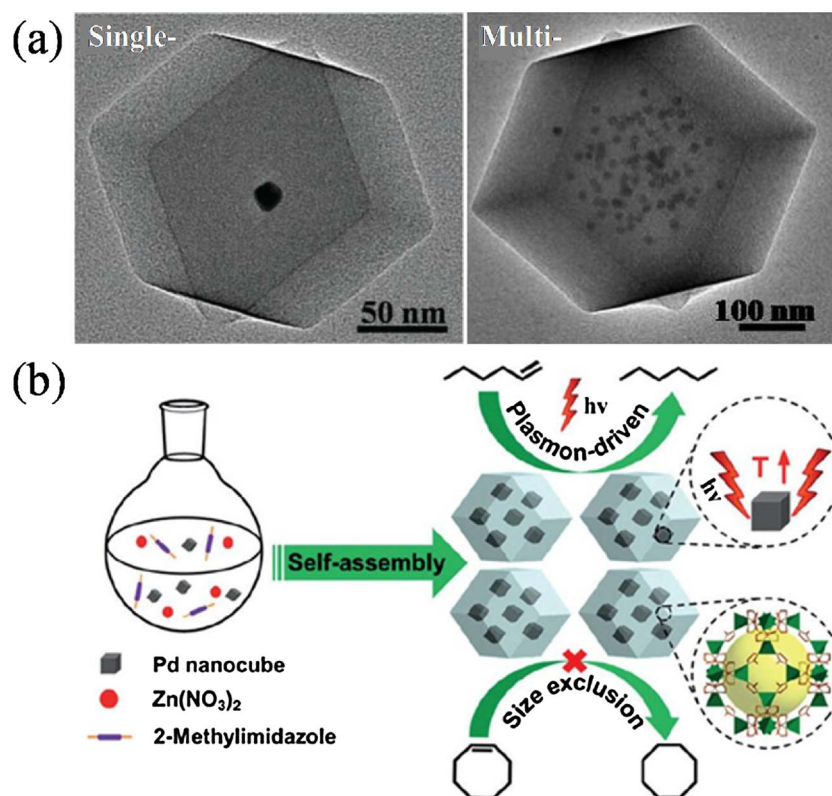


Fig. 25. TEM images of Au@ZIF-8 single- or multi-core-shell structures [243] (a) and self-assembly of Pd NCs@ZIF-8 and plasmon-driven selective catalysis of the hydrogenation of olefins [242] (b).

Table 5
Photocatalytic CO₂ reduction performance promoted with various MOFs [246].

MOFs	CO (μmol)	H ₂ (μmol)	CO + H ₂ (μmol)	Sel.CO (%)
Co-ZIF-67	29.6	14.8	44.4	66.7
Zn-ZIF-8	1.8	2.0	3.8	47.4
Cu-MOF	1.2	1.5	2.7	44.4
Zr-Uio-66-NH ₂	0.9	1.2	2.1	42.9
Fe-MIL-101-NH ₂	4.7	2.1	6.8	69.1

in the N-doped graphene analogs could also be well-tuned through the calcination. The N-doped graphene analogs derived from ZIF-8 calcined at 1000 °C exhibited the highest photocatalytic activity for H₂ production from water splitting due to the existence of the highest content of graphitic nitrogen. In 2017, an extraordinary ZnO@C-N-Co core-shell

nanocomposite was constructed by directly pyrolyzing a hollow Zn/Co-ZIF matrix consisting of a ZIF-8 shell with some Co-ZIF nanoplates inside the hollow cavity at 600 °C under an argon atmosphere [253]. Interestingly, the ZIF-8-shell-derived ZnO NPs could agglomerate spontaneously and move to the hollow cavity while the internal Co NPs transferred inversely to the linker-derived N-C shell during the pyrolysis process (Fig. 26). The unique composites showed a remarkable photocatalytic activity and excellent recyclability for the degradation of MO. Meanwhile, Pt-ZnO-Co₃O₄ was also constructed by pyrolysis of bimetallic ZnCo-ZIFs followed by doping Pt NPs [254]. Compared to the ZIF-8 and ZIF-67-based derivatives, Pt-ZnO-Co₃O₄ had a higher photocatalytic hydrogen generation rate.

Recently, two-step pyrolysis of ZIF-8 to produce ZnO for photocatalysis was also investigated. Compared with ZnO prepared via one-step pyrolysis, two-step pyrolytic ZnO possesses lots of merits, including

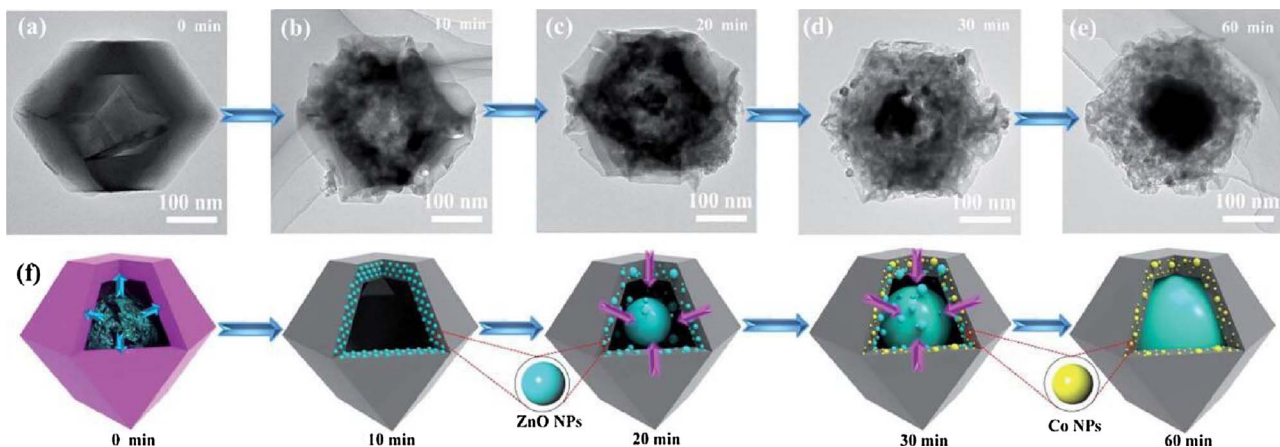


Fig. 26. TEM images of the products collected at different pyrolysis times (a–e) and Schematic illustration of the formation process of the core-shell ZnO@C-N-Co (f) [253].

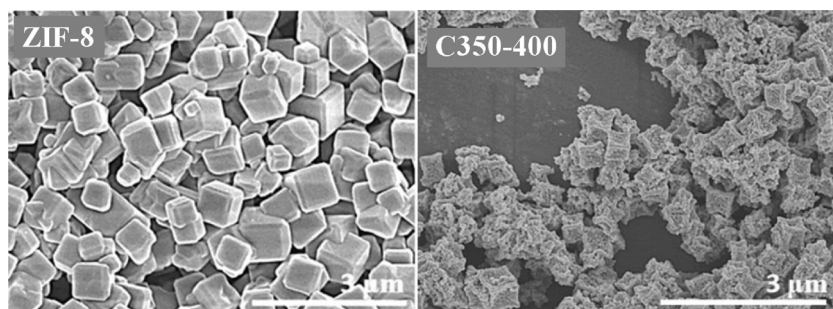


Fig. 27. SEM images of pristine ZIF-8 and C350-400 sample [255].

the higher surface area, more amounts of C doping and higher optical absorption. More importantly, the two-step calcined samples showed much higher photocatalytic activity than that of one-step calcined samples [255–257]. In 2016, Pan and co-workers prepared C-doped ZnO by two-step calcination of ZIF-8 (SEM images are shown in Fig. 27) and the sample C350-400 (C-doped ZnO, firstly calcined at 350 °C for 2 h, then 400 °C for 1 h) showed an increased photoactivity that was about three-fold and four-fold higher than ZnO (C450) in photocatalytic degradation of RhB and photoelectrochemical (PEC) water splitting under UV-vis irradiation [255]. Liang and co-workers also synthesized C, N-doped ZnO by two-step pyrolysis of ZIF-8 [256,257]. Firstly, ZIF-8 carbonization in a nitrogen atmosphere limited Zn into porous carbon, and the followed calcination in air formed nanosized ZnO photocatalysts. The hybrids were evaluated by photocatalytic degradation of MB and oxygen evolution reaction (OER). However, the two-step pyrolysis is more complex than one-step pyrolysis relatively.

5.6. Incorporation with other functional materials

A hybrid composite ZIF-8/black phosphorus (BP) was composed of ZIF-8 NPs uniformly distributed on the surface of BP nanosheets [258]. BP functionalized with polyvinylpyrrolidone (PVP) was promoted for the in situ growth of ZIF-8, and the pyrrolidone rings (C=O) enhanced the affinity between Zn ions and BP. The obtained nanocomposites exhibited excellent catalytic efficiency on photocatalytic degradation of MB. Activation of peroxymonosulfate (PMS) represents a widely-used chemical oxidation reaction for chemical synthesis and environmental remediation. Lin and co-workers used ZIF-67 to activate PMS and the degradation activity of RhB was enhanced under UV-light irradiation [259].

Although the large band gap energy and low CB potential of ZIF-8 limited its applications in photocatalysis, the regular topological structure, rapid synthesis and easy to control of ZIF-8 still attract huge attention in photocatalytic fields. The modified strategies of ZIFs and their corresponding applications are listed in Table 6.

6. Other MOFs

Most of studies focused on the modification to above-mentioned three types MOFs (UiOs, MILs and ZIFs). A primary reason is that their good stability. The above MOF-based photocatalysts could retain crystallinity and activity at least three recycles in water, weak acid and base according to the previous reports [36,37,70,260,261]. Except the major three types of MOFs, there are still a small number of other stable MOFs modified for photocatalysis, e.g. HKUST-1 [262–267], NTU-9 [268].

HKUST-1 is composed of 1, 3, 5-benzenetricarboxylate linkers coordinating with copper ions in a cubic lattice. It possesses a relatively large band gap that is more than 3 eV [266,267]. In 2014, Abedi and co-workers prepared a stable mesoporous HKUST-1 via a surfactant-assisted templating method [262]. After a suitable amount of amorphous titania (70 wt%) incorporated into the meso-HKUST-1, the conversion of sunlight-driven selective aerobic photooxidation could reach 100%

and the corresponding selectivity was 99%. Mosleh's research group has done lots of work based on HKUST-1 for photocatalysis. They prepared BiPO₄/Bi₂S₃-HKUST-1 composites and applied it in a catalytic rotating packed bed reactor [264]. The toluidine blue and auramine-O in the reactor could be simultaneous photocatalytic degradation under visible-light illumination. Later, they synthesized Ag₃PO₄/AgBr/Ag-HKUST-1 instead of BiPO₄/Bi₂S₃-HKUST-1 as photocatalysts and realized the simultaneous degradation of ternary mixture (MB, auramine-O and erythrosine) [265]. The research group of Majid also prepared Ag₂CrO₄/HKUST-1 [266] and Ag/Ag₃PO₄/HKUST-1 [267] composites for the photocatalytic degradation of azo dyes Congo Red and Ponceau BS. Pyrolyzation had been used in HKUST-1 as well. Zhang and co-workers developed magnetic Fe₃O₄@C/Cu and Fe₃O₄@CuO nanocomposites with a core/shell structure via direct calcinations of Fe₃O₄@HKUST-1 in N₂ and air respectively [263]. Results demonstrated that the Fe₃O₄@C/Cu performed obvious activity in the degradation of MB under visible-light illumination in the presence of H₂O₂ compared with Fe₃O₄@CuO nanocomposites, TiO₂ and g-C₃N₄. After the first synthesis of NTU-9, Kaur and co-workers firstly modified NTU-9 by mixing CdTe quantum dots in its formation liquid. The prepared composites showed enhanced activity for the visible-light driven photocatalytic degradation of rhodamine 6G.

7. Conclusions and outlook

Various MOFs have emerged as photocatalysts, where pristine MOFs were introduced from UV-light response to visible-light response, and MOFs modifications were developed in the following aspects: decoration of organic linker or metal center, combination with semiconductors, MNPs loading, decoration with RGO, sensitization, pyrolyzation and incorporation with other functional materials. Although intense work has been carried out to investigate MOFs for photocatalysis, mainly concentrating on UiO-66(Zr), MIL-125(Ti) and ZIF-8(Zn), because they are robust enough to survive harsh catalytic conditions and possess perfect crystal structures. However, these MOFs lack redox-activities and visible-light response, which limited their applications and photocatalytic efficiency under visible-light irradiations. The photocatalytic applications mainly focused on H₂ production, CO₂ reduction and environmental remediation. Few MOFs were used for photocatalytic organic synthesis. In addition, MOFs are normally synthesized by a solvothermal method with raw materials that are expensive compared to conventional photocatalysts (e.g. TiO₂) and the stability is still a problem. Hence, MOFs as photocatalysts for practical applications are promising but remain a great challenge.

To combat these aforementioned problems, several approaches could be attempted: 1) as metals like Fe and Co have the redox-activities and visible-light response, the research hotspots will likely transfer to visible-light responsive MILs (MIL-101(Co), MIL-100(Fe) and MIL-53(Fe)) for photocatalysis. 2) More modified MOFs as photocatalysts should be tried to use in organic synthesis reactions, such as oxidation of alcohol, Suzuki reaction and even hydrogenative cyclization. 3) Improving synthetic efficiency for existing MOFs and developing new

Table 6

Modified strategies of ZIFs and their corresponding applications.

Strategies	Details	MOF	Applications	Light source	Ref.
Partial substitution of metal center	Cu	ZIF-67	MO degradation	Visible	[233]
	Ni	ZIF-8	MB degradation	Visible	[234]
Combination with semiconductors	ZnO	ZIF-8	Cr(VI) reduction	UV	[236]
	ZnO	ZIF-8	MB degradation	UV	[235]
Zn ₂ GeO ₄	ZnO	K ₂ P ₂ W ₁₈ O ₆₂ /ZIF-8	MB, RhB degradation	UV-vis	[237]
	Zn ₂ GeO ₄	ZIF-8	CO ₂ reduction	UV-vis	[232]
g-C ₃ N ₄	g-C ₃ N ₄	ZIF-8	CO ₂ reduction	UV-vis	[239]
	g-C ₃ N ₄	ZIF-8	Tetracycline degradation	Sunlight	[240]
TiO ₂	TiO ₂	ZIF-8	RhB degradation	UV	[215]
	TiO ₂	ZIF-8	Cr(VI) reduction	UV-vis	[238]
Cu ₇ S ₄	Cu ₇ S ₄	ZIF-8	Cyclocondensation	Laser	[241]
	Cu _{0.5} Zn _{0.5} S	ZIF-8	Cr(VI) reduction	Visible	[111]
MNPs loading	Ag	AgCl/ZIF-8	RhB, MB degradation	Visible	[217–219]
	Au	ZIF-8	Alcohols oxidation	Visible	[243]
	Pd	ZIF-8	Olefins hydrogenation	UV-vis	[242]
Sensitization	[Ru(bpy) ₃]Cl ₂ ·6H ₂ O	ZIF-67	CO ₂ reduction	Visible	[246]
	RuN ₃	ZIF-67	H ₂ production	Visible	[245]
Pyrolyzation	ZnO	ZIF-8	CO ₂ reduction	UV-vis	[251]
	(C-ZIF)/g-C ₃ N ₄	Melamine/ZIF-8	H ₂ production	Visible	[250]
	C,N doped ZnO	ZIF-8	MB degradation, oxygen evolution	Visible	[256]
	ZnO@C-N-Co	Zn/Co-ZIF	MO degradation	UV-vis	[253]
	N-doped ZnO	Urea/ZIF-8	RhB degradation	Visible	[231]
	N-doped ZNG	ZIF-8	H ₂ production	UV-vis	[252]
	C-doped ZnO	ZIF-8	RhB degradation and PEC water splitting	UV-vis	[255]
	C-N-ZnO	ZIF-8	MB degradation and OER	UV-vis	[257]
	Pt-ZnO-Co ₃ O ₄	Zn/Co-ZIF	H ₂ production	UV-vis	[254]

MOFs that contain redox active metals (e.g., Co, Ni, Mn, Fe) and/or functional organic linkers (e.g., imidazolate, porphyrin, pyridine) are worthy of study. 4) Adding some template agent in the corresponding synthesis solutions is a desirable way to further improve the crystallinity and stability of MOFs [28]. It is noticed that constructing multi-functional MOF photocatalysts is an interesting but tough work, which means that the oxidation reaction and the reduction reaction occur simultaneously on both sides. Up to now, Cr(VI) reduction and dyes oxidation have been realized in one system [62,95,209]. Multi-functional MOF photocatalysts are required in the more advanced reactions in one system, such as water splitting/CO₂ reduction. All in all, MOF-mediated photocatalysts currently are still in their infancy and hold a great potential in energy regeneration and environmental remediation in the future. We anticipate that this review will provide an essential resource for guiding both academic and industrial research to design or select the most appropriate photocatalytic materials.

Acknowledgments

The authors are grateful for the financial support of Natural Science Key Project of the Jiangsu Higher Education Institutions (15KJA220001), Jiangsu Province Six Talent Peaks Project (2016-XCL-043), National Natural Science Foundation of China (NNSFC, 21706134), and Priority Academic Program Development of Jiangsu Higher Education Institutions (PAPD). J.Q. thanks the financial support from the Doctorate Fellowship Foundation of Nanjing Forestry University.

References

- [1] A. Fujishima, K. Honda, *Nature* 238 (1972) 37–38.
- [2] S.C. Yan, Z.S. Li, Z.G. Zou, *Langmuir* 25 (2009) 10397–10401.
- [3] C. Chen, W. Ma, J. Zhao, *Chem. Soc. Rev.* 39 (2010) 4206–4219.
- [4] L.J. Shen, L.J. Huang, S.J. Liang, R.W. Liang, N. Qin, L. Wu, *RSC Adv.* 4 (2014) 2546–2549.
- [5] H. Chen, C.E. Nanayakkara, V.H. Grassian, *Chem. Rev.* 112 (2012) 5919–5948.
- [6] Z.G. Zou, J.H. Ye, K. Sayama, H. Arakawa, *Nature* 414 (2001) 625–627.
- [7] A. Kudo, Y. Miseki, *Chem. Soc. Rev.* 38 (2009) 253–278.
- [8] W. Tu, Y. Zhou, Z. Zou, *Adv. Mater.* 26 (2014) 4607–4626.
- [9] P. Li, Y. Zhou, Z. Zhao, Q. Xu, X. Wang, M. Xiao, Z. Zou, *J. Am. Chem. Soc.* 137 (2015) 9547–9550.
- [10] X. Chen, A. Selloni, *Chem. Rev.* 114 (2014) 9281–9282.
- [11] G. Liu, H.G. Yang, J. Pan, Y.Q. Yang, G.Q. Lu, H.-M. Cheng, *Chem. Rev.* 114 (2014) 9559–9612.
- [12] R. Asahi, T. Morikawa, T. Ohwaki, K. Aoki, Y. Taga, *Science* 293 (2001) 269–271.
- [13] H. Zhang, X.J. Lv, Y.M. Li, Y. Wang, J.H. Li, *ACS Nano* 4 (2010) 380–386.
- [14] S. Yan, Z. Li, Z. Zou, *Langmuir* 25 (2009) 10397–10401.
- [15] F. Dong, Z. Zhao, T. Xiong, Z. Ni, W. Zhang, Y. Sun, W.-K. Ho, *ACS Appl. Mater. Interfaces* 5 (2013) 11392–11401.
- [16] S. Cao, J. Low, J. Yu, M. Jaroniec, *Adv. Mater.* 27 (2015) 2150–2176.
- [17] N. Daneshvar, D. Salari, A.R. Khataee, *J. Photochem. Photobiol. A* 162 (2004) 317–322.
- [18] K. Maeda, T. Takata, M. Hara, N. Saito, Y. Inoue, H. Kobayashi, K. Domen, *J. Am. Chem. Soc.* 127 (2005) 8286–8287.
- [19] Y. Liu, L. Fang, H. Lu, L. Liu, H. Wang, C. Hu, *Catal. Commun.* 17 (2012) 200–204.
- [20] H. Wang, Y. Bai, J. Yang, X. Lang, J. Li, L. Guo, *Chem-Eur. J.* 18 (2012) 5524–5529.
- [21] Y. Wang, R. Shi, J. Lin, Y. Zhu, *Energy Environ. Sci.* 4 (2011) 2922–2929.
- [22] S. Kumar, T. Surendar, A. Baruah, V. Shanker, *J. Mater. Chem. A* 1 (2013) 5333–5340.
- [23] H. Furukawa, N. Ko, Y.B. Go, N. Aratani, S.B. Choi, E. Choi, A.Ö. Yazaydin, R.Q. Snurr, M. O’Keeffe, J. Kim, *Science* 329 (2010) 424–428.
- [24] A.J. Cooper, M.J. Rosseinsky, *Nat. Chem.* 1 (2009) 26–27.
- [25] A.R. Millward, O.M. Yaghi, *J. Am. Chem. Soc.* 127 (2005) 17998–17999.
- [26] J.L. Rowell, O.M. Yaghi, *Angew. Chem. Int. Ed.* 44 (2005) 4670–4679.
- [27] J. Yao, H. Wang, *Chem. Soc. Rev.* 43 (2014) 4470–4493.
- [28] J. Qiu, Y. Feng, X. Zhang, M. Jia, J. Yao, *J. Colloid Interface Sci.* 499 (2017) 151–158.
- [29] M. Jia, Y. Feng, S. Liu, J. Qiu, J. Yao, *J. Membr. Sci.* 539 (2017) 172–177.
- [30] P. Horcajada, T. Chalati, C. Serre, B. Gillet, C. Sebrie, T. Baati, J.F. Eubank, D. Heurtaux, P. Clayette, C. Kreuz, *Nat. Mater.* 9 (2010) 172–178.
- [31] L.E. Kreno, K. Leong, O.K. Farha, M. Allendorf, R.P. Van Duyne, J.T. Hupp, *Chem. Rev.* 112 (2011) 1105–1125.
- [32] J. Lee, O.K. Farha, J. Roberts, K.A. Scheidt, S.T. Nguyen, J.T. Hupp, *Chem. Soc. Rev.* 38 (2009) 1450–1459.
- [33] A. Dhakshinamoorthy, M. Alvaro, H. Garcia, *Chem. Commun.* 48 (2012) 11275–11288.
- [34] J. Qiu, M. He, M. Jia, J. Yao, *Prog. Chem.* 28 (2016) 1016–1028.
- [35] L. Shen, G. Wang, X. Zheng, Y. Cao, Y. Guo, K. Lin, L. Jiang, *Chin. J. Catal.* 38 (2017) 1373–1381.
- [36] T. Zhang, W. Lin, *Chem. Soc. Rev.* 43 (2014) 5982–5993.
- [37] S.B. Wang, X.C. Wang, *Small* 11 (2015) 3097–3112.
- [38] F.X. Llabrés i Xamena, O. Casanova, R. Galiasso Tailleur, H. Garcia, A. Corma, *J. Catal.* 255 (2008) 220–227.
- [39] F.X. Llabrés i Xamena, A. Corma, H. Garcia, *J. Phys. Chem. C* 111 (2007) 80–85.
- [40] J. Gao, J. Miao, P.-Z. Li, W.Y. Teng, L. Yang, Y. Zhao, B. Liu, Q. Zhang, *Chem. Commun.* 50 (2014) 3786–3788.
- [41] L.J. Shen, S.J. Liang, W.M. Wu, R.W. Liang, L. Wu, *J. Mater. Chem. A* 1 (2013) 11473–11482.
- [42] J. He, J.Q. Wang, Y.J. Chen, J.P. Zhang, D.L. Duan, Y. Wang, Z.Y. Yan, *Chem. Commun.* 50 (2014) 7063–7066.

[43] Y.P. Yuan, L.S. Yin, S.W. Cao, G.S. Xu, C.H. Li, C. Xue, *Appl. Catal. B-Environ.* 168 (2015) 572–576.

[44] C. Gomes Silva, I. Luz, F.X. Llabrés i Xamena, A. Corma, H. García, *Chem-Eur. J.* 16 (2010) 11133–11138.

[45] Y. Fu, D. Sun, Y. Chen, R. Huang, Z. Ding, X. Fu, Z. Li, *Angew. Chem. Int. Ed.* 51 (2012) 3364–3367.

[46] D. Guo, R.Y. Wen, M.M. Liu, H.X. Guo, J.H. Chen, W. Weng, *Appl. Organomet. Chem.* 29 (2015) 690–697.

[47] X. Chen, S. Shen, L. Guo, S.S. Mao, *Chem. Rev.* 110 (2010) 6503–6570.

[48] N. Serpone, A. Emeline, *J. Phys. Chem. Lett.* 3 (2012) 673–677.

[49] V. Coropeceanu, J. Cornil, D.A. da Silva Filho, Y. Olivier, R. Silbey, J.-L. Brédas, *Chem. Rev.* 107 (2007) 926–952.

[50] L. Kaake, P.F. Barbara, X.-Y. Zhu, *J. Phys. Chem. Lett.* 1 (2010) 628–635.

[51] J.-J. Du, Y.-P. Yuan, J.-X. Sun, F.-M. Peng, X. Jiang, L.-G. Qiu, A.-J. Xie, Y.-H. Shen, J.-F. Zhu, *J. Hazard. Mater.* 190 (2011) 945–951.

[52] M. Alvaro, E. Carbonell, B. Ferrer, F.X. Llabrés i Xamena, H. García, *Chem-Eur. J.* 13 (2007) 5106–5112.

[53] P. Mahata, G. Madras, S. Natarajan, *J. Phys. Chem. B* 110 (2006) 13759–13768.

[54] J. Gascon, M.D. Hernández-Alonso, A.R. Almeida, G.P. Van Klink, F. Kapteijn, G. Mul, *ChemSusChem* 1 (2008) 981–983.

[55] T. Tachikawa, J.R. Choi, M. Fujitsuka, T. Majima, *J. Phys. Chem. C* 112 (2008) 14090–14101.

[56] S. Hausdorf, Jr., W. Wagler, R. Moßig, F.O. Mertens, *J. Phys. Chem. A* 112 (2008) 7567–7576.

[57] S. Pu, L. Xu, L. Sun, H. Du, *Inorg. Chem. Commun.* 52 (2015) 50–52.

[58] H.-P. Jing, C.-C. Wang, Y.-W. Zhang, P. Wang, R. Li, *RSC Adv.* 4 (2014) 54454–54462.

[59] M. Dan-Hardi, C. Serre, T. Frot, L. Rozes, G. Maurin, C. Sanchez, G. Férey, *J. Am. Chem. Soc.* 131 (2009) 10857–10859.

[60] P. George, N.R. Dhabarde, P. Chowdhury, *Mater. Lett.* 186 (2017) 151–154.

[61] M.C. Das, H. Xu, Z. Wang, G. Srinivas, W. Zhou, Y.-F. Yue, V.N. Nesterov, G. Qian, B. Chen, *Chem. Commun.* 47 (2011) 11715–11717.

[62] R.W. Liang, F.F. Jing, L.J. Shen, N. Qin, L. Wu, *J. Hazard. Mater.* 287 (2015) 364–372.

[63] C. Zhang, L. Ai, J. Jiang, *J. Mater. Chem. A* 3 (2015) 3074–3081.

[64] Y. Gao, S. Li, Y. Li, L. Yao, H. Zhang, *Appl. Catal. B-Environ.* 202 (2017) 165–174.

[65] D. Wang, M. Wang, Z. Li, *ACS Catal.* 5 (2015) 6852–6857.

[66] E.A. Kozlova, V.N. Panchenko, Z. Hasan, N.A. Khan, M.N. Timofeeva, S.H. Jhung, *Catal. Today* 266 (2016) 136–143.

[67] C.Y. Lee, O.K. Farha, B.J. Hong, A.A. Sarjeant, S.T. Nguyen, J.T. Hupp, *J. Am. Chem. Soc.* 133 (2011) 15858–15861.

[68] K.G. Laurier, F. Vermoortele, R. Ameloot, D.E. De Vos, J. Hofkens, M.B. Roeffaers, *J. Am. Chem. Soc.* 135 (2013) 14488–14491.

[69] L. Chi, Q. Xu, X. Liang, J. Wang, X. Su, *Small* 12 (2016) 1351–1358.

[70] Y. Li, H. Xu, S. Ouyang, J. Ye, *Phys. Chem. Chem. Phys.* 18 (2016) 7563–7572.

[71] R. Trujillano, F. Villain, C. Louis, J.-F. Lambert, *J. Phys. Chem. C* 111 (2007) 7152–7164.

[72] B. Pattengale, S. Yang, J. Ludwig, Z. Huang, X. Zhang, J. Huang, *J. Am. Chem. Soc.* 138 (2016) 8072–8075.

[73] H. Park, D.A. Reddy, Y. Kim, R. Ma, J. Choi, T.K. Kim, K.-S. Lee, *Solid State Sci.* 62 (2016) 82–89.

[74] A. Schaate, P. Roy, A. Godt, J. Lippke, F. Waltz, M. Wiebcke, P. Behrens, *Chem-Eur. J.* 17 (2011) 6643–6651.

[75] J.H. Cavka, S. Jakobsen, U. Olsbye, N. Guillou, C. Lamberti, S. Bordiga, K.P. Lillerud, *J. Am. Chem. Soc.* 130 (2008) 13850–13851.

[76] S. Wang, W. Yao, J. Lin, Z. Ding, X. Wang, *Angew. Chem. Int. Ed.* 53 (2014) 1034–1038.

[77] Y. Lee, S. Kim, J.K. Kang, S.M. Cohen, *Chem. Commun.* 51 (2015) 5735–5738.

[78] L.J. Shen, S.J. Liang, W.M. Wu, R.W. Liang, L. Wu, *Dalton Trans.* 42 (2013) 13649–13657.

[79] T.W. Goh, C. Xiao, R.V. Maligal-Ganesh, X. Li, W. Huang, *Chem. Eng. Sci.* 124 (2015) 45–51.

[80] K. Hendrickx, D.E.P. Vanpoucke, K. Leus, K. Lejaeghere, A. Van Yperen-De Deyne, V. Van Speybroeck, P. Van Der Voort, K. Hemelsoet, *Inorg. Chem.* 54 (2015) 10701–10710.

[81] L.J. Shen, R.W. Liang, M.B. Luo, F.F. Jing, L. Wu, *Phys. Chem. Chem. Phys.* 17 (2015) 117–121.

[82] D. Sun, W. Liu, M. Qiu, Y. Zhang, Z. Li, *Chem. Commun.* 51 (2015) 2056–2059.

[83] A. Santiago Portillo, H.G. Baldovi, M.T. Garcia Fernandez, S. Navalon, P. Atienzar, B. Ferrer, M. Alvaro, H. García, Z. Li, *J. Phys. Chem. C* 121 (2017) 7015–7024.

[84] J.P. Tu, X.L. Zeng, F.J. Xu, X. Wu, Y.F. Tian, X.D. Hou, Z. Long, *Chem. Commun.* 53 (2017) 3361–3364.

[85] R. Lin, L.J. Shen, Z.Y. Ren, W.M. Wu, Y.X. Tan, H.R. Fu, J. Zhang, L. Wu, *Chem. Commun.* 50 (2014) 8533–8535.

[86] L.J. Shen, M.B. Luo, Y.H. Liu, R.W. Liang, F.F. Jing, L. Wu, *Appl. Catal. B-Environ.* 166 (2015) 445–453.

[87] J.-J. Zhou, R. Wang, X.-L. Liu, F.-M. Peng, C.-H. Li, F. Teng, Y.-P. Yuan, *Appl. Surf. Sci.* 346 (2015) 278–283.

[88] Y. Su, Z. Zhang, H. Liu, Y. Wang, *Appl. Catal. B-Environ.* 200 (2017) 448–457.

[89] Z. Sha, J.L. Sun, H.S.O. Chan, S. Jaenicke, J.S. Wu, *RSC Adv.* 4 (2014) 64977–64984.

[90] Z. Sha, H.S.O. Chan, J.S. Wu, *J. Hazard. Mater.* 299 (2015) 132–140.

[91] Z. Sha, J.S. Wu, *RSC Adv.* 5 (2015) 39592–39600.

[92] L. Shi, T. Wang, H.B. Zhang, K. Chang, J.H. Ye, *Adv. Funct. Mater.* 25 (2015) 5360–5367.

[93] J. Ding, Z. Yang, C. He, X. Tong, Y. Li, X. Niu, H. Zhang, *J. Colloid Interface Sci.* 497 (2017) 126–133.

[94] Q. Liang, M. Zhang, Z. Zhang, C. Liu, S. Xu, Z. Li, *J. Alloy. Compd.* 690 (2017) 123–130.

[95] L. Shen, W. Wu, R. Liang, R. Lin, L. Wu, *Nanoscale* 5 (2013) 9374–9382.

[96] D. Sun, Z. Li, *J. Phys. Chem. C* 120 (2016) 19744–19750.

[97] E.H. Otal, M.L. Kim, M.E. Calvo, L. Karvonen, I.O. Fabregas, C.A. Sierra, J.P. Hinestroza, *Chem. Commun.* 52 (2016) 6665–6668.

[98] J. Xu, S. He, H. Zhang, J. Huang, H. Lin, X. Wang, J. Long, *J. Mater. Chem. A* 3 (2015) 24261–24271.

[99] E. Flage-Larsen, A. Royset, J.H. Cavka, K. Thorshaug, *J. Phys. Chem. C* 117 (2013) 20610–20616.

[100] T. Musho, J. Li, N. Wu, *Phys. Chem. Chem. Phys.* 16 (2014) 23646–23653.

[101] D. Azarifar, R. Ghorbani-Vaghei, S. Daliran, A.R. Oveisi, *Chemcatchem* 9 (2017) 1992–2000.

[102] A.S. Yasin, J. Li, N. Wu, T. Musho, *Phys. Chem. Chem. Phys.* 18 (2016) 12748–12754.

[103] I. Tsuji, H. Kato, H. Kobayashi, A. Kudo, *J. Am. Chem. Soc.* 126 (2004) 13406–13413.

[104] Y. Huang, Z. Zheng, Z. Ai, L. Zhang, X. Fan, Z. Zou, *J. Phys. Chem. B* 110 (2006) 19323–19328.

[105] S. Das, H. Kim, K. Kim, *J. Am. Chem. Soc.* 131 (2009) 3814–3815.

[106] M. Kim, J.F. Cahill, H. Fei, K.A. Prather, S.M. Cohen, *J. Am. Chem. Soc.* 134 (2012) 18082–18088.

[107] D. Jing, L. Guo, *J. Phys. Chem. B* 110 (2006) 11139–11145.

[108] D. Meissner, R. Memming, B. Kastening, *J. Phys. Chem. 92* (1988) 3476–3483.

[109] J. Yu, Z. Zhang, M. Jaroniec, *Green Chem.* 12 (2010) 1611–1614.

[110] Q. Li, H. Meng, P. Zhou, Y. Zheng, J. Wang, J. Yu, J. Gong, *ACS Catal.* 3 (2013) 882–889.

[111] J. Qiu, X.-F. Zhang, X. Zhang, Y. Feng, Y. Li, L. Yang, H. Lu, J. Yao, *J. Hazard. Mater.* 349 (2018) 234–241.

[112] X. Meng, Z. Zhang, *J. Mol. Catal. A-Chem.* 423 (2016) 533–549.

[113] Z. Sha, J. Sun, H.S.O. Chan, S. Jaenicke, J. Wu, *Chemppluschem* 80 (2015) 1321–1328.

[114] H. Gan, Z. Wang, H. Li, Y. Wang, L. Sun, Y. Li, *RSC Adv.* 6 (2016) 5192–5197.

[115] X. Hao, Z. Jin, H. Yang, G. Lu, Y. Bi, *Appl. Catal. B-Environ.* 210 (2017) 45–56.

[116] A. Crake, K.C. Christoforidis, A. Kafizas, S. Zafeiratos, C. Petit, *Appl. Catal. B-Environ.* 210 (2017) 131–140.

[117] X. Xu, R. Liu, Y. Cui, X. Liang, C. Lei, S. Meng, Y. Ma, Z. Lei, Z. Yang, *Appl. Catal. B-Environ.* 210 (2017) 484–494.

[118] X. Wang, K. Maeda, A. Thomas, K. Takanabe, G. Xin, J.M. Carlsson, K. Domen, M. Antonietti, *Nat. Mater.* 8 (2009) 76–80.

[119] X. Chen, J. Zhang, X. Fu, M. Antonietti, X. Wang, *J. Am. Chem. Soc.* 131 (2009) 11658–11659.

[120] M. Stratakis, H. García, *Chem. Rev.* 112 (2012) 4469–4506.

[121] H. Goesmann, C. Feldmann, *Angew. Chem. Int. Ed.* 49 (2010) 1362–1395.

[122] B. O'regan, M. Grifitzi, *Nature* 353 (1991) 737–740.

[123] H. Tributsch, *Coord. Chem. Rev.* 248 (2004) 1511–1530.

[124] J. Pyun, *Angew. Chem. Int. Ed.* 50 (2011) 46–48.

[125] C.H. Henton, D. Tiana, M. Fontecave, C. Sanchez, L. D'Arras, C. Sassoye, L. Rozes, C. Mellot-Draznieks, A. Walsh, *J. Am. Chem. Soc.* 135 (2013) 10942–10945.

[126] D. Sun, L. Ye, Z. Li, *Appl. Catal. B-Environ.* 164 (2015) 428–432.

[127] M.B. Chambers, X. Wang, L. Ellezam, O. Ersen, M. Fontecave, C. Sanchez, L. Rozes, C. Mellot-Draznieks, *J. Am. Chem. Soc.* 139 (2017) 8222–8228.

[128] J.G. Santaclara, M.A. Nasalevich, S. Castellanos, W.H. Evers, F.C.M. Spoor, K. Rock, L.D.A. Siebelles, F. Kapteijn, F. Grozema, A. Houtepen, J. Gascon, J. Hunger, M.A. van der Veen, *Chemsuschem* 9 (2016) 388–395.

[129] H. Wang, X. Yuan, Y. Wu, G. Zeng, X. Chen, L. Leng, Z. Wu, L. Jiang, H. Li, J. Hazard. Mater. 286 (2015) 187–194.

[130] M.W. Logan, Y.A. Lau, Y. Zheng, E.A. Hall, M.A. Hettinger, R.P. Marks, M.L. Hosler, F.M. Rossi, Y. Yuan, F.J. Uribe-Romo, *Catal. Sci. Technol.* 6 (2016) 5647–5655.

[131] J. Luo, F. Xu, J. Tu, X. Wu, X. Hou, *Microchem. J.* 132 (2017) 245–250.

[132] X. Lian, B. Yan, *Inorg. Chem.* 55 (2016) 11831–11838.

[133] M.W. Logan, S. Ayad, J.D. Adamson, T. Dilbeck, H.B. Kenneth, F.J. Uribe-Romo, *J. Mater. Chem. A* 5 (2017) 11854–11863.

[134] S. Abedi, A. Morsali, *New J. Chem.* 39 (2015) 931–937.

[135] S. Hu, M. Liu, K. Li, C. Song, G. Zhang, X. Guo, *RSC Adv.* 7 (2017) 581–587.

[136] H. Wang, X. Yuan, Y. Wu, G. Zeng, X. Chen, L. Leng, H. Li, *Appl. Catal. B-Environ.* 174 (2015) 445–454.

[137] Y.-P. Zhu, M. Li, Y.-L. Liu, T.-Z. Ren, Z.-Y. Yuan, *J. Phys. Chem. C* 118 (2014) 10963–10971.

[138] Z. Yang, X. Xu, X. Liang, C. Lei, Y. Cui, W. Wu, Y. Yang, Z. Zhang, Z. Lei, *Appl. Catal. B-Environ.* 205 (2017) 42–54.

[139] J. Xu, J. Gao, C. Wang, Y. Yang, L. Wang, *Appl. Catal. B-Environ.* 219 (2017) 101–108.

[140] T. Di, B. Zhu, B. Cheng, J. Yu, J. Xu, *J. Catal.* 352 (2017) 532–541.

[141] G. Zhou, M.-F. Wu, Q.-J. Xing, F. Li, H. Liu, X.-B. Luo, J.-P. Zou, J.-M. Luo, A.-Q. Zhang, *Appl. Catal. B-Environ.* 220 (2018) 607–614.

[142] A.V. Vinogradov, H. Zaake-Hertling, E. Hey-Hawkins, A.V. Agafonov, G.A. Seisenbaeva, V.G. Kessler, V.V. Vinogradov, *Chem. Commun.* 50 (2014) 10210–10213.

[143] D.O. Jin, Q. Xu, L.Y. Yu, X.Y. Hu, *Microchim. Acta.* 182 (2015) 1885–1892.

[144] H. Wang, X. Yuan, Y. Wu, G. Zeng, H. Dong, X. Chen, L. Leng, Z. Wu, L. Peng, *Appl. Catal. B-Environ.* 186 (2016) 19–29.

[145] S.-R. Zhu, P.-F. Liu, M.-K. Wu, W.-N. Zhao, G.-C. Li, K. Tao, F.-Y. Yi, L. Han, *Dalton Trans.* 45 (2016) 17521–17529.

[146] N.A. Rodriguez, A. Savateev, M.A. Grela, D. Dontsova, *ACS Appl. Mater. Interfaces* (2017).

[147] C.T. Hou, Q. Xu, Y.J. Wang, X.Y. Hu, *RSC Adv.* 3 (2013) 19820–19823.

[148] D. Sun, W. Liu, Y. Fu, Z. Fang, F. Sun, X. Fu, Y. Zhang, Z. Li, *Chem-Eur. J.* 20 (2014) 4780–4788.

[149] L. Shen, M. Luo, L. Huang, P. Feng, L. Wu, *Inorg. Chem.* 54 (2015) 1191–1193.

[150] Y. Horiuchi, T. Toyao, M. Saito, K. Mochizuki, M. Iwata, H. Higashimura, M. Anpo, M. Matsuo, *J. Phys. Chem. C* 116 (2012) 20848–20853.

[151] R.M. Abdellameed, M.M.Q. Simoes, A.M.S. Silva, J. Rocha, *Chem-Eur. J.* 21 (2015) 11072–11081.

[152] X.Z. Yuan, H. Wang, Y. Wu, G.M. Zeng, X.H. Chen, L.J. Leng, Z.B. Wu, H. Li, *Appl. Organomet. Chem.* 30 (2016) 289–296.

[153] H. Guo, D. Guo, Z. Zheng, W. Weng, J. Chen, *Appl. Organomet. Chem.* 29 (2015) 618–623.

[154] Y. Fu, L. Sun, H. Yang, L. Xu, F. Zhang, W. Zhu, *Appl. Catal. B-Environ.* 187 (2016) 212–217.

[155] K. Meyer, S. Bashir, J. Llorca, H. Idriss, M. Ranocchiari, J.A. van Bokhoven, *Chem-Eur. J.* 22 (2016) 13894–13899.

[156] H. Frenzel, A. Lajn, M. Brandt, H. von Wenckstern, G. Biehne, H. Hochmuth, M. Lorenz, M. Grundmann, *Appl. Phys. Lett.* (2008) 92.

[157] X. Xie, Y. Li, Z.-Q. Liu, M. Haruta, W. Shen, *Nature* 458 (2009) 746–749.

[158] N. Zheng, G.D. Stucky, *J. Am. Chem. Soc.* 128 (2006) 14278–14280.

[159] Y. Wang, H. Lu, Y. Wang, J. Qiu, J. Wen, K. Zhou, L. Chen, G. Song, J. Yao, *RSC Adv.* 6 (2016) 1860–1864.

[160] H. Lu, B. Zhao, R. Pan, J. Yao, J. Qiu, L. Luo, Y. Liu, *RSC Adv.* 4 (2014) 1128–1132.

[161] H. Li, Y. Hao, H. Lu, L. Liang, Y. Wang, J. Qiu, X. Shi, Y. Wang, J. Yao, *Appl. Surf. Sci.* 344 (2015) 112–118.

[162] J. Qiu, Y. Feng, X. Zhang, X. Zhang, M. Jia, J. Yao, *RSC Adv.* 7 (2017) 10668–10674.

[163] T.Y. Ma, S. Dai, M. Jaroniec, S.Z. Qiao, *J. Am. Chem. Soc.* 136 (2014) 13925–13931.

[164] Z. Guo, J.K. Cheng, Z. Hu, M. Zhang, Q. Xu, Z. Kang, D. Zhao, *RSC Adv.* 4 (2014) 34221–34225.

[165] K. Khaletskaya, A. Pougin, R. Medishetty, C. Rosler, C. Wiktor, J. Strunk, R.A. Fischer, *Chem. Mater.* 27 (2015) 7248–7257.

[166] J. Dou, Y. Li, F. Xie, X. Ding, M. Wei, *Cryst. Growth Des.* 16 (2016) 121–125.

[167] J.L. Li, X.T. Xu, X.J. Liu, W. Qin, M. Wang, L.K. Pan, *J. Alloy. Compd.* 690 (2017) 640–646.

[168] J. Li, X. Xu, X. Liu, W. Qin, L. Pan, *Ceram. Int.* 43 (2017) 835–840.

[169] M.A. Nasalevich, M.G. Goesten, T.J. Savenije, F. Kapteijn, J. Gascon, *Chem. Commun.* 49 (2013) 10575–10577.

[170] L.Z. Huang, B.S. Liu, *RSC Adv.* 6 (2016) 17873–17879.

[171] M.A. Nasalevich, R. Becker, E.V. Ramos-Fernandez, S. Castellanos, S.L. Veber, M.V. Fedin, F. Kapteijn, J.N.H. Reek, J.I. van der Vlugt, J. Gascon, *Energy Environ. Sci.* 8 (2015) 364–375.

[172] Z. Li, J.-D. Xiao, H.-L. Jiang, *ACS Catal.* 6 (2016) 5359–5365.

[173] G. Ferey, C. Mellot-Draznieks, C. Serre, F. Millange, J. Dutour, S. Surble, I. Margioliaki, *Science* 309 (2005) 2040–2042.

[174] J. He, Z. Yan, J. Wang, J. Xie, L. Jiang, Y. Shi, F. Yuan, F. Yu, Y. Sun, *Chem. Commun.* 49 (2013) 6761–6763.

[175] N.V. Maksimchuk, K.A. Kovalenko, V.P. Fedin, O.A. Kholdeeva, *Adv. Synth. Catal.* 352 (2010) 2943–2948.

[176] Y. Xu, Q. Chen, H. Yang, M. Lv, Q. He, X. Liu, F. Wei, *Mat. Sci. Semicon. Proc.* 36 (2015) 115–123.

[177] S. Gao, T. Feng, C. Feng, N. Shang, C. Wang, *J. Colloid Interface Sci.* 466 (2016) 284–290.

[178] X. Li, Y. Pi, Q. Xia, Z. Li, J. Xiao, *Appl. Catal. B-Environ.* 191 (2016) 192–201.

[179] D. Tilgner, R. Kempe, *Chem-Eur. J.* 23 (2017) 3184–3190.

[180] X.-L. Si, L.-x. Sun, F. Xu, C.-l. Jiao, F. Li, S.-s. Liu, J. Zhang, L.-f. Song, C.-h. Jiang, S. Wang, Y.-L. Liu, Y. Sawada, *Int. J. Hydrom. Energy* 36 (2011) 6698–6704.

[181] P. Horcajada, S. Surble, C. Serre, D.-Y. Hong, Y.-K. Seo, J.-S. Chang, J.-M. Grenche, I. Margioliaki, G. Ferey, *Chem. Commun.* (2007) 2820–2822.

[182] F. Ke, L. Wang, J. Zhu, *Nano Res.* 8 (2015) 1834–1846.

[183] K.G.M. Laurier, F. Vermoortele, R. Ameloot, D.E. De Vos, J. Hofkens, M.B.J. Roeffaers, *J. Am. Chem. Soc.* 135 (2013) 14488–14491.

[184] T. Loiseau, C. Serre, C. Huguenard, G. Fink, F. Taulelle, M. Henry, T. Bataille, G. Ferey, *Chem-Eur. J.* 10 (2004) 1373–1382.

[185] C. Serre, F. Millange, C. Thouvenot, M. Nogues, G. Marsolier, D. Louer, G. Ferey, *J. Am. Chem. Soc.* 124 (2002) 13519–13526.

[186] P. Horcajada, C. Serre, G. Maurin, N.A. Ramsahye, F. Balas, M. Vallet-Regi, M. Sebban, F. Taulelle, G. Ferey, *J. Am. Chem. Soc.* 130 (2008) 6774–6780.

[187] E. Haque, N.A. Khan, J.H. Park, S.H. Jhung, *Chem-Eur. J.* 16 (2010) 1046–1052.

[188] L. Shi, T. Wang, H.B. Zhang, K. Chang, X.G. Meng, H.M. Liu, J.H. Ye, *Adv. Sci.* 2 (2015).

[189] Y. An, H. Li, Y. Liu, B. Huang, Q. Sun, Y. Dai, X. Qin, X. Zhang, *J. Solid. State. Chem.* 233 (2016) 194–198.

[190] N. Chang, H. Zhang, M.-S. Shi, J. Li, W. Shao, H.-T. Wang, *Mater. Lett.* 200 (2017) 55–58.

[191] Z. Jiang, J. Liu, M. Gao, X. Fan, L. Zhang, J. Zhang, *Adv. Mater.* (2017) 29.

[192] D. Tilgner, M. Friedrich, J. Hermannsdoerfer, R. Kempe, *Chemcatchem* 7 (2015) 3916–3922.

[193] J. Han, D. Wang, Y. Du, S. Xi, Z. Chen, S. Yin, T. Zhou, R. Xu, *Appl. Catal. A* 521 (2016) 83–89.

[194] H. Gao, W. Zhen, J. Ma, G. Lu, *Appl. Catal. B-Environ.* 206 (2017) 353–363.

[195] J. He, H. Yang, Y. Chen, Z. Yan, Y. Zeng, Z. Luo, W. Gao, J. Wang, *Water Air Soil Pollut.* (2015) 226.

[196] R. Liang, S. Luo, F. Jing, L. Shen, N. Qin, L. Wu, *Appl. Catal. B-Environ.* 176 (2015) 240–248.

[197] J. Hong, C. Chen, F.E. Bedoya, G.H. Kelsall, D. O'Hare, C. Petit, *Catal. Sci. Technol.* 6 (2016) 5042–5051.

[198] J. Zheng, Z. Jiao, *J. Colloid Interf. Sci.* 488 (2016) 234–239.

[199] X. Liu, R. Dang, W. Dong, X. Huang, J. Tang, H. Gao, G. Wang, *Appl. Catal. B-Environ.* 209 (2017) 506–513.

[200] J. Yang, X. Niu, S. An, W. Chen, J. Wang, W. Liu, *RSC Adv.* 7 (2017) 2943–2952.

[201] M. Wen, K. Mori, T. Kamegawa, H. Yamashita, *Chem. Commun.* 50 (2014) 11645–11648.

[202] X.-L. Liu, R. Wang, M.-Y. Zhang, Y.-P. Yuan, C. Xue, *Apl. Mater.* (2015) 3.

[203] Y. Wu, H. Luo, L. Zhang, *Environ. Sci. Pollut. R.* 22 (2015) 17238–17243.

[204] M. Wen, Y. Kuwahara, K. Mori, H. Yamashita, *Top. Catal.* 59 (2016) 1765–1771.

[205] J. Yan, W.-Z. Zhou, H. Tan, X.-J. Feng, Y.-H. Wang, Y.-G. Li, *Crystengcomm* 18 (2016) 8762–8768.

[206] W. Zhen, H. Gao, B. Tian, J. Ma, G. Lu, *ACS Appl. Mater. Inter.* 8 (2016) 10808–10819.

[207] R. Liang, F. Jing, L. Shen, N. Qin, L. Wu, *Nano Res.* 8 (2015) 3237–3249.

[208] D. Wang, Z. Li, *J. Catal.* 342 (2016) 151–157.

[209] R.W. Liang, L.J. Shen, F.F. Jing, N. Qin, L. Wu, *ACS Appl. Mater. Interfaces* 7 (2015) 9507–9515.

[210] C.H. Zhang, L.H. Ai, J. Jiang, *Ind. Eng. Chem. Res.* 54 (2015) 153–163.

[211] Z. Yang, X. Xu, X. Liang, C. Lei, Y. Wei, P. He, B. Lv, H. Ma, Z. Lei, *Appl. Catal. B-Environ.* 198 (2016) 112–123.

[212] Y. Yang, W. Wang, H. Li, X. Jin, H. Wang, L. Zhang, Y. Zhang, *Mater. Lett.* 197 (2017) 17–20.

[213] C.-F. Zhang, L.-G. Qiu, F. Ke, Y.-J. Zhu, Y.-P. Yuan, G.-S. Xu, X. Jiang, *J. Mater. Chem. A* 1 (2013) 14329–14334.

[214] H. Zhao, L. Qian, H. Lv, Y. Wang, G. Zhao, *Chemcatchem* 7 (2015) 4148–4155.

[215] X. Zeng, L. Huang, C. Wang, J. Wang, J. Li, X. Luo, *ACS Appl. Mater. Interfaces* 8 (2016) 20274–20282.

[216] R. Liang, R. Chen, F. Jing, N. Qin, L. Wu, *Dalton Trans.* 44 (2015) 18227–18236.

[217] S.T. Gao, W.H. Liu, N.Z. Shang, C. Feng, Q.H. Wu, Z. Wang, C. Wang, *RSC Adv.* 4 (2014) 61736–61742.

[218] J. Liu, R. Li, Y. Hu, T. Li, Z. Jia, Y. Wang, X. Zhang, C. Fan, *Appl. Catal. B-Environ.* 202 (2017) 64–71.

[219] J. Liu, R. Li, Y. Wang, X. Zhang, C. Fan, *J. Alloy. Compd.* 693 (2017) 543–549.

[220] W. Guo, H. Lv, Z. Chen, K.P. Sullivan, S.M. Lauinger, Y. Chi, J.M. Sumliner, T. Lian, C.L. Hill, *J. Mater. Chem. A* 4 (2016) 5952–5957.

[221] R. Bashyam, P. Zelenay, *Nature* 443 (2006) 63–66.

[222] C. Karunakaran, P. Vinayagamoorthy, J. Jayabharathi, *Langmuir* 30 (2014) 15031–15039.

[223] T. Araya, M. Jia, J. Yang, P. Zhao, K. Cai, W. Ma, Y. Huang, *Appl. Catal. B-Environ.* 203 (2017) 768–777.

[224] M. Li, Z. Zheng, Y. Zheng, C. Cui, C. Li, Z. Li, *ACS Appl. Mater. Interfaces* 9 (2017) 2899–2905.

[225] X. Feng, H. Chen, F. Jiang, *J. Colloid Interface Sci.* 494 (2017) 32–37.

[226] G. Xu, J. Yao, K. Wang, L. He, P.A. Webley, C.-s. Chen, H. Wang, *J. Membrane Sci.* 385 (2011) 187–193.

[227] R. Chen, J. Yao, Q. Gu, S. Smeets, C. Baerlocher, H. Gu, D. Zhu, W. Morris, O.M. Yaghi, H. Wang, *Chem. Commun.* 49 (2013) 9500–9502.

[228] L. Li, J. Yao, P. Xiao, J. Shang, Y. Feng, P.A. Webley, H. Wang, *Colloid Polym. Sci.* 291 (2013) 2711–2717.

[229] Y. Li, K. Zhou, M. He, J. Yao, *Microporous Mesoporous Mater.* 234 (2016) 287–292.

[230] H. Wang, F.X. Yin, B.H. Chen, X.B. He, P.L. Lv, C.Y. Ye, D.J. Liu, *Appl. Catal. B-Environ.* 205 (2017) 55–67.

[231] Y. Feng, H. Lu, X. Gu, J. Qiu, M. Jia, C. Huang, J. Yao, *J. Phys. Chem. Solids* 102 (2017) 110–114.

[232] Q. Liu, Z.-X. Low, L. Li, A. Razmjou, K. Wang, J. Yao, H. Wang, *J. Mater. Chem. A* 1 (2013) 11563–11569.

[233] H. Yang, X.-W. He, F. Wang, Y. Kang, J. Zhang, *J. Mater. Chem. B* 22 (2012) 21849–21851.

[234] R. Li, X. Ren, H. Ma, X. Feng, Z. Lin, X. Li, C. Hu, B. Wang, *J. Mater. Chem. A* 2 (2014) 5724–5729.

[235] B. Yu, F. Wang, W. Dong, J. Hou, P. Lu, J. Gong, *Mater. Lett.* 156 (2015) 50–53.

[236] X.B. Wang, J. Liu, S. Leong, X.C. Lin, J. Wei, B. Kong, Y.F. Xu, Z.X. Low, J.F. Yao, H.T. Wang, *ACS Appl. Mater. Interfaces* 8 (2016) 9080–9087.

[237] B. Hong, L. Liu, S.-M. Wang, Z.-B. Han, *J. Clust. Sci.* 27 (2016) 563–571.

[238] Q. Liu, B. Zhou, M. Xu, G. Mao, *RSC Adv.* 7 (2017) 8004–8010.

[239] S. Liu, F. Chen, S. Li, X. Peng, Y. Xiong, *Appl. Catal. B-Environ.* 211 (2017) 1–10.

[240] S. Panneri, M. Thomas, P. Ganguly, B.N. Nair, A.P. Mohamed, K.G.K. Warrier, U.S. Hareesh, *Catal. Sci. Technol.* 7 (2017) 2118–2128.

[241] F. Wang, Y. Huang, Z. Chai, M. Zeng, Q. Li, Y. Wang, D. Xu, *Chem. Sci.* 7 (2016) 6887–6893.

[242] Q. Yang, Q. Xu, S.H. Yu, H.L. Jiang, *Angew. Chem. Int. Ed.* 55 (2016) 3685–3689.

[243] L. Chen, Y. Peng, H. Wang, Z. Gua, C. Duana, *Chem. Commun.* 50 (2014) 8651–8654.

[244] R. Jiang, B. Li, C. Fang, J. Wang, *Adv. Mater.* 26 (2014) 5274–5309.

[245] S. Yang, B. Pattengale, E.L. Kovrigin, J. Huang, *Accs Energy Lett.* 2 (2017) 75–80.

[246] J. Qin, S. Wang, X. Wang, *Appl. Catal. B-Environ.* 209 (2017) 476–482.

[247] L. Schmidt-Mende, J.L. MacManus-Driscoll, *Mater. Today* 10 (2007) 40–48.

[248] K. Park, Q. Zhang, B.B. Garcia, X. Zhou, Y.-H. Jeong, G. Cao, *Adv. Mater.* 22 (2010) 2329–2332.

[249] W. Yu, J. Zhang, T. Peng, *Appl. Catal. B-Environ.* 181 (2016) 220–227.

[250] F. He, G. Chen, Y.S. Zhou, Y.G. Yu, L.Q. Li, S. Hao, B. Liu, *J. Mater. Chem. A* 4 (2016) 3822–3827.

[251] S. Liu, J. Wang, J. Yu, *RSC Adv.* 6 (2016) 59998–60006.

[252] X. Zhao, H. Yang, P. Jing, W. Shi, G. Yang, P. Cheng, *Small* 13 (2017).

[253] H. Chen, K. Shen, J. Chen, X. Chen, Y. Li, *J. Mater. Chem. A* 5 (2017) 9937–9945.

[254] M. Lan, R.-M. Guo, Y. Dou, J. Zhou, A. Zhou, J.-R. Li, *Nano Energy* 33 (2017) 238–246.

[255] L. Pan, T. Muhammad, L. Ma, Z.F. Huang, S.B. Wang, L. Wang, J.J. Zou, X.W. Zhang, *Appl. Catal. B-Environ.* 189 (2016) 181–191.

[256] P. Liang, C. Zhang, H. Sun, S. Liu, M. Tade, S. Wang, *RSC Adv.* 6 (2016) 95903–95909.

[257] P. Liang, C. Zhang, H. Sun, S. Liu, M. Tade, S. Wang, *Energ. Fuel.* 31 (2017) 2138–2143.

[258] L. Wang, Q. Xu, J. Xu, J. Weng, *RSC Adv.* 6 (2016) 69033–69039.

[259] K.-Y.A. Lin, H.-A. Chang, *J. Taiwan Inst. Chem. E.* 53 (2015) 40–45.

[260] J.-L. Wang, C. Wang, W. Lin, *ACS Catal.* 2 (2012) 2630–2640.

[261] L. Shen, R. Liang, L. Wu, *Chin. J. Catal.* 36 (2015) 2071–2088.

[262] S. Abedi, A. Morsali, *ACS Catal.* 4 (2014) 1398–1403.

[263] Y.-F. Zhang, L.-G. Qiu, Y.-P. Yuan, Y.-J. Zhu, X. Jiang, J.-D. Xiao, *Appl. Catal. B-Environ.* 144 (2014) 863–869.

[264] S. Mosleh, M.R. Rahimi, M. Ghaedi, K. Dashtian, S. Hajati, *RSC Adv.* 6 (2016) 63667–63680.

[265] S. Mosleh, M.R. Rahimi, M. Ghaedi, K. Dashtian, S. Hajati, S. Wang, *Chem. Eng. Process.* 114 (2017) 24–38.

[266] O. Mehraj, F.A. Sofi, S.K. Moosvi, W. Naqash, K. Majid, *J. Mater. Sci. Mater. Electron.* 29 (2018) 3358–3369.

[267] F.A. Sofi, K. Majid, O. Mehraj, *J. Alloy. Compd.* 737 (2018) 798–808.

[268] R. Kaur, A. Rana, R.K. Singh, V.A. Chhabra, K.-H. Kim, A. Deep, *RSC Adv.* 7 (2017) 29015–29024.